

Pore-scale characterization of carbon dioxide storage at immiscible and near-miscible conditions in altered-wettability reservoir rocks



Abdulla Alhosani ^{a,*}, Qingyang Lin ^a, Alessio Scanziani ^a, Edward Andrews ^a, Kaiqiang Zhang ^b, Branko Bijeljic ^a, Martin J. Blunt ^a

^a Imperial College London, Department of Earth Science and Engineering, London, UK

^b Imperial College London, Department of Chemical Engineering, London, UK

ARTICLE INFO

Keywords:

Carbon dioxide capture and storage (CCS)
Enhanced oil recovery (EOR)
Immiscible and near-miscible CO₂ injection
conditions
X-ray micro-tomography (micro-CT)
Three-phase flow in porous media

ABSTRACT

Carbon dioxide storage combined with enhanced oil recovery (CCS-EOR) is an important approach for reducing greenhouse gas emissions. We use pore-scale imaging to help understand CO₂ storage and oil recovery during CCS-EOR at immiscible and near-miscible CO₂ injection conditions. We study *in situ* immiscible CO₂ flooding in an oil-wet reservoir rock at elevated temperature and pressure using X-ray micro-tomography. We observe the predicted, but hitherto unreported, three-phase wettability order in strongly oil-wet rocks, where water occupies the largest pores, oil the smallest, while CO₂ occupies pores of intermediate size. We investigate the pore occupancy, existence of CO₂ layers, recovery and CO₂ trapping in the oil-wet rock at immiscible conditions and compare to the results obtained on the same rock type under slightly more weakly oil-wet near-miscible conditions, with the same wettability order. CO₂ spreads in connected layers at near-miscible conditions, while it exists as disconnected ganglia in medium-sized pores at immiscible conditions. Hence, capillary trapping of CO₂ by oil occurs at immiscible but not at near-miscible conditions. Moreover, capillary trapping of CO₂ by water is not possible in both cases since CO₂ is more wetting to the rock than water. The oil recovery by CO₂ injection alone is reduced at immiscible conditions compared to near-miscible conditions, where low gas-oil capillary pressure improves microscopic displacement efficiency. Based on these results, to maximize the amount of oil recovered and CO₂ stored at immiscible conditions, a water-alternating-gas injection strategy is suggested, while a strategy of continuous CO₂ injection is recommended at near-miscible conditions.

1. Introduction

Capture and geological storage of CO₂ (CCS) is one of the most promising options in the portfolio of mitigation actions for the reduction of atmospheric greenhouse gas emissions (Bruant et al., 2002; Pacala and Socolow, 2004; Metz et al., 2005; Edenhofer, 2015; First, 2018). In CCS, carbon dioxide is captured from major stationary sources and transported to the storage site, where CO₂ is injected in deep geological formations. Among the various geological formations suitable for carbon dioxide storage, depleted oil and gas reservoirs are considered the most economical and practical short term solution due to their large storage capacity and existent injection facilities (Heidug et al., 2015; Stewart et al., 2018; Núñez-López et al., 2019). Moreover, the injection of CO₂ in oil reservoirs has the economic advantage of coupling CCS with enhanced oil recovery (EOR). During CO₂-EOR, there is a simultaneous flow of three fluid phases, oil, water and CO₂, in the pore spaces of the

reservoir rock. Hence, understanding the physics behind three-phase flow in porous media is essential to control the local displacement efficiency in CCS-EOR projects in terms of the amount of CO₂ stored and oil recovered.

Most three-phase flow studies have focussed on quantifying the relative permeabilities of oil, gas and water at the centimetre-scale (Leverett and Lewis, 1941; Sarem, 1966; Saraf et al., 1982; Oak, 1990; DiCarlo et al., 2000; Alizadeh and Piri, 2014; Kianinejad and DiCarlo, 2016). The relative permeability of each fluid phase is a strong function of the size of the pores occupied by that phase at the pore-scale (Blunt, 2017). That is, if a phase occupies large and/or intermediate sized pores, it will flow more readily compared to if it occupies smaller pores. At the pore-scale, the pore occupancy of each phase is dependent on the wettability order of the system, which in turn is a function of the rock surface wettability and miscibility. The most wetting phase tends to reside close to the solid surface and in small pores, while the most

* Corresponding author.

E-mail address: Abdulla.alhosani17@imperial.ac.uk (A. Alhosani).

non-wetting phase preferentially fills the centres of the larger pores. In an oil reservoir, the wettability of the rock surface can either be water-wet, weakly oil-wet or strongly oil-wet, or a mixture of water-wet and oil-wet regions, known as mixed-wettability (van Dijke and Sorbie, 2002).

For a water-wet rock at immiscible gas injection conditions, the wettability order is water-oil-gas from most to least wetting, where water, the most wetting phase, occupies the pore corners and/or small sized pores, gas, the most non-wetting phase, resides in the centres and/or large sized pores, while oil, the intermediate-wet phase, spreads in layers between water and gas, while occupying the centres of intermediate-sized pores (Scanziani et al., 2018b; Oren et al., 1992). This wettability order is altered under immiscible weakly oil-wet conditions, as oil becomes the most wetting phase then water then gas (oil-water-gas) (Scanziani et al., 2018a; Qin et al., 2019). This wettability order, with gas remaining the most non-wetting phase and hence having a high relative permeability, is consistent with the results of several flooding experiments (Blunt, 2017). For strongly oil-wet rocks, it is predicted that the wettability order changes: while oil remains the most wetting phase, gas becomes the intermediate-wet phase and water the most non-wetting phase (van Dijke and Sorbie, 2002; Blunt, 2017). Nonetheless, to date, there has been no direct experimental evidence of this wettability order inside rock samples under immiscible three-phase flow conditions, although this has been observed in micro-model experiments (Sohrabi et al., 2004).

However, the order of wettabilities described above is only pertinent at immiscible gas injection conditions, representing low reservoir pressures, or a heavy oil, where the interfacial tension between oil and gas is high, that is of the order 10 mN/m or more. However, in many gas injection projects, to optimize recovery, the gas and oil are frequently near-miscible with a gas-oil interfacial tension of order 1 mN/m or less. A recent study by Alhosani et al. (2019) has demonstrated that for a water-wet system, the strict wettability order breaks down at near-miscible conditions as oil and gas both become neutrally wetting to the rock surface, while water remains the most wetting phase. Furthermore, Alhosani et al. (2020b) have shown that for oil-wet near-miscible conditions, the wettability order is altered again such that gas becomes the intermediate-wet phase spreading in layers, oil becomes the most wetting phase, while water becomes the most non-wetting phase.

In addition to controlling the fluid relative permeabilities, the wettability order of the system plays a significant role in determining the storage security of carbon dioxide in the reservoir by means of capillary trapping. Capillary or residual trapping occurs when CO₂ becomes surrounded by water (or oil) as a disconnected bubble in the centres of the pore space (Krevor et al., 2015; Andrew et al., 2014c). Therefore, for CO₂ to become trapped by another fluid phase in the centres of the pore space, in general it must be less wetting than that phase.

Recent advances in 3D X-ray imaging (micro-CT) have permitted the direct visualization of *in situ* wettability order inside the pore space during three-phase flow experiments – at high pressure and temperature reservoir conditions – which has allowed many scientists to investigate the mechanisms of capillary trapping in a system with three fluid phases (Blunt et al., 2013; Wildenschild and Sheppard, 2013; Brown et al., 2014; Scanziani et al., 2018b, a; Scanziani et al., 2019; Alhosani et al., 2019; Qin et al., 2019; Iglauer et al., 2019; Alhosani et al., 2020b; Scanziani et al., 2020a; Blunt et al., 2021).

Scanziani et al. (2018b) and Qin et al. (2019) used micro-CT imaging to investigate capillary trapping of the gas phase in water-wet and weakly oil-wet carbonate oil reservoirs, respectively. Scanziani et al. (2018b) reported that, at immiscible conditions in a water-wet system, gas was trapped as disconnected blobs in the centre of the pore space surrounded by oil layers and there was no direct trapping of gas by water when oil was present. This was attributed to the spreading of oil layers which prevents direct gas-water contact in the pore space. Overall, there was enhanced gas trapping under three-phase conditions, as oil is now

strongly wetting to gas. On the other hand, Qin et al. (2019) reported that, at immiscible conditions in a weakly oil-wet system, gas was trapped by both water and oil phases. This was ascribed to the direct gas-water and gas-oil contacts in the pore space, since water, the intermediate-wet phase, does not spread in layers, which allows the trapping of gas by oil. Both studies concluded that gas trapping was enhanced under three-phase conditions compared to two-phase gas-water systems, indicating that capillary trapping provides a fast and secure mechanism to retain gas in the subsurface of oil reservoirs.

Nonetheless, to accurately assess the efficiency of carbon dioxide storage in oil reservoirs, we need to study the role of wettability order in oil-wet rocks. This is particularly important since many carbonate reservoirs, which contain over half the world's reserves of conventional oil, often tend to be strongly oil-wet (Blunt, 2017). The presence of crude oil in the pore space of the rocks under high temperature and pressure for such long periods exposes the rock surfaces to severe wettability alteration, *i.e.* all surfaces contacted by oil are expected to be rendered oil-wet (Kovscek et al., 1993; Buckley, 2001).

In this work, we provide the first experimental evidence of the anticipated three-phase wettability order in oil-wet rocks at immiscible conditions – using micro-tomography X-ray imaging – and assess the implications it has on the safety of carbon dioxide storage in CO₂-EOR applications. We perform an immiscible water-alternating-gas (WAG) micro-CT flow experiment in a carbonate reservoir rock at elevated temperature and pressure (60 °C and 8 MPa). We examine, *in situ*, (i) fluid-fluid geometric contact angles, (ii) pore occupancy, (iii) fluid configurations and connectivity (Euler characteristic), (iv) three-phase capillary pressures, (v) presence or absence of gas layers, (vi) specific interfacial areas, (vii) fluid saturations and (viii) CO₂ trapping mechanisms. We compare the results with previous measurements on an oil-wet reservoir rock under near-miscible conditions with the same wettability order – oil-gas-water from most to least wetting – Alhosani et al. (2020b). This work can contribute to designing an optimal CO₂ injection strategy to maximize the amount of CO₂ stored and oil recovered at both immiscible and near-miscible conditions in CCS-EOR projects.

2. Materials and methods

2.1. Rock and fluid properties

The rock selected for study was extracted from a giant producing carbonate hydrocarbon reservoir in the Middle East, with a mineralogical composition of 96.5 % ± 1.9 % calcite, 1.5 % ± 0.3 % dolomite, 1.1 % ± 0.2 % kaolinite and 0.8 % ± 0.4 % quartz (Alhammadi et al., 2017). The cylindrical rock sample was 6.1 mm in diameter and 24.6 mm in length. The petrophysical properties of the sample are listed in Table 1. The segmented X-ray porosity was lower than the total helium porosity as it considers the macro-porosity only, leaving out the micro-porosity within the rock grains which cannot be imaged. We assume that the micro-porosity remains fully water saturated throughout the experiment. The sample was drilled from the same larger piece of rock and is of similar size to the sample used by Alhosani et al. (2020b) in the near-miscible study.

The three fluid phases used in the experiment were: (i) light crude oil from the same reservoir as the rock (refer to Table 2 for the crude oil

Table 1
Petrophysical properties of the reservoir sample.

Sample properties		
Diameter	6.1	mm
Length	24.6	mm
Total helium porosity	26.1	%
Segmented X-ray porosity	18.0	%
Pore volume (PV)	187	µL

Table 2

Composition analysis of the reservoir crude oil. Data from Alhammadi et al. (2017).

Crude oil properties		
Density at 21 °C	830 ± 5	kg/m ³
Saturates	55.25	wt%
Aromatics	38.07	wt%
Resins	6.22	wt%
Asphaltenes	0.46	wt%
Total Acid Number	0.24	mg KOH/g
Total Base Number	356	ppm

properties); (ii) brine solution prepared using the same salt composition as the reservoir brine; and (iii) supercritical (sc) CO₂. Both crude oil and brine were doped with contrast agents, 20 wt% iododecane (C₁₀H₂₁I) and 30 wt% sodium iodide (NaI) respectively, to enhance the contrast between the phases in the pore-scale images. This allows us to accurately differentiate between the different fluids and rock in the images and is essential to obtain an effective subsequent image segmentation (Andrew et al., 2014c).

The interfacial tensions between the selected experimental fluids, water (70 wt% brine + 30 wt% sodium iodide), oil (80 wt% crude oil + 20 wt% iododecane) and supercritical CO₂, scCO₂, were measured using the pendant drop method at two-phase equilibrium. The apparatus for conducting the interfacial tension measurements at the experimental conditions (60 °C and 8 MPa) is detailed elsewhere (Li et al., 2012): it took approximately 10 min for the fluids to reach equilibrium. The thermophysical properties of the fluids used in this experiment are shown in Table 3. Furthermore, the properties of the fluids used by Alhosani et al. (2020b) in the near-miscible study are shown in Table S1 in the supplementary material.

2.2. Ageing protocol

To restore the original reservoir surface wettability, the rock sample was placed in contact with crude oil in a process called ageing (Salathiel, 1973; Kovsek et al., 1993; Alhammadi et al., 2017; Alhosani et al., 2020a; Scanziani et al., 2020b). The ageing process was carried out both: (i) dynamically, where the rock sample was continuously flooded with crude oil at high temperature and pressure (80 °C and 10 MPa); and (ii) statically, where the rock was placed in a crude oil bath at high temperature only (80 °C). The dynamic ageing procedure consisted of the following steps:

- 1 Firstly, the rock was cleaned using methanol and dried at 80 °C in an oven for 24 h.
- 2 Reservoir brine was injected into the sample (100% brine saturation) and the temperature and pressure were elevated to reservoir conditions, 80 °C and 10 MPa. The brine was pre-equilibrated with crushed pieces of the same carbonate rock as the experimental sample to avoid any chemical reactions during the ageing process.

Table 3

Thermophysical properties of the three fluid phases selected for the experiment at 60 °C and 8 MPa. The gas spreading coefficient at the experimental conditions was calculated using $C_{sg} = \sigma_{ow} - \sigma_{gw} - \sigma_{go}$, where o, w and g label oil, water and gas respectively. Data from NIST (2019); CDP (2020) and Toolbox (2020). *Densities measured at ambient conditions, 20 °C and 0.1 MPa.

Fluid	Composition (%wt)	ρ (kg·m ⁻³)	μ (mPa·s)	σ (mN·m ⁻¹)
Water	70 % brine + 30 % Sodium Iodide	1414.9*	0.468	$\sigma_{gw} = 30.98$
Oil	80 % crude oil + 20 % Iododecane	890.5*	0.305	$\sigma_{ow} = 21.23$
Gas	scCO ₂	191.6	0.023	$\sigma_{go} = 9.75$ $C_{sg} = -19.5$

- 3 40 pore volumes (PV) of crude oil were injected from the bottom of the sample with a stepwise increase in the flow rate from 0.001 mL/min to 0.1 mL/min.
- 4 The flow direction was then reversed, and 40 PV of crude oil were injected from the top of the sample at the same flow rates.
- 5 Subsequent to saturating the sample with crude oil, five PV of crude oil were then injected every day into the sample for a week.
- 6 The sample was then maintained at the high pressure and temperature (80 °C and 10 MPa) established initially for another three weeks with no flow.

After dynamically ageing the sample for four weeks, the sample was immersed in a sealed crude oil bath and left to age statically at high temperature, 80 °C, for eight months in this study.

2.3. Flow apparatus and flooding experiment

After restoring the reservoir wettability in the rock, the sample was prepared for the flooding experiment. The sample was initially wrapped with aluminium foil and then tightly fitted in a cylindrical Viton sleeve, as shown in Fig. 1. The bottom and top ends of the sample were then connected to the inlet and outlet flow lines respectively. The sample and flow lines were assembled inside a Hassler type carbon fibre coreholder. The coreholder was placed in a ZEISS Xradia 510 Versa 3D micro-CT scanner for image acquisition during the flow experiment, while the rest of the apparatus was assembled outside, see Fig. 1.

The flow apparatus consisted of: (i) four Teledyne Isco pumps, to inject the reservoir fluids at high pressures (8 MPa); (ii) a coreholder, to keep the rock under pressure (10 MPa) with a confining fluid (water); (iii) a flexible heater connected to a PID controller, to raise and maintain the temperature of the sample at the experimental conditions (60 °C); and (iv) a Parr stirred reactor, to equilibrate the scCO₂, brine and rock phases at the experimental conditions prior to injection. Equilibrating scCO₂ and brine with crushed fragments of the rock is an essential step to avoid the formation of acidic brine, a product of scCO₂ and brine mixing, which can dissolve the carbonate rock during the experiment. Therefore, the fluids and rock were vigorously mixed in the reactor for at least 24 h prior to any injection to attain chemical equilibrium between the fluids. Both scCO₂ and brine were injected directly from the reactor.

During the flow experiment, three injections were performed to simulate a water-alternating-gas (WAG) flooding strategy, which is the typical displacement sequence encountered in oilfields (Lake, 1989). The injections were performed in the following order: (i) first waterflooding [WF1]; (ii) gas injection [GI]; and (iii) second waterflooding [WF2]. All injections were performed from the bottom of the sample under capillary dominated conditions to represent flow in the centre of the field away from the wellbore, see Table 4. This is the same flooding sequence adopted by Alhosani et al. (2020b) in the near-miscible flooding experiment. The steps adopted to perform the experiment were as follows:

- 1 To initiate the experiment, 50 PV of doped crude oil (80 wt% crude oil + 20 wt% Iododecane) were flushed through the rock at a flow rate of 0.1 mL/min to replace the undoped crude oil in the aged sample.
- 2 The pressure in the sample was then raised gradually to the experimental pressure (8 MPa), and the confining pressure to 10 MPa. A confining pressure was applied to ensure the flow is restricted to the vertical direction only and prevent any fluid bypassing along the sample walls.
- 3 The sample temperature was then elevated to the experimental conditions (60 °C) using the heating jacket.
- 4 The WAG flooding sequence was then started by injecting 2 PV of water into the rock at a rate of 0.005 mL/min for 75 min., this was followed by the injection of 2 PV of scCO₂ and then 2 PV of water at the same flow rate.

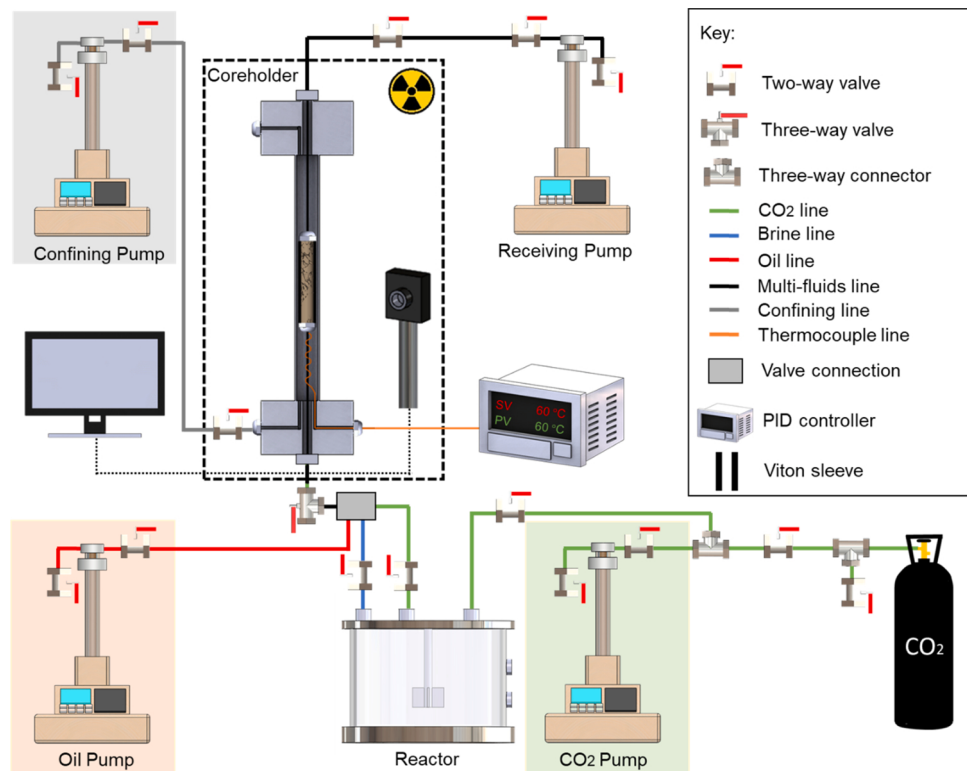


Fig. 1. The flow apparatus used to conduct the three-phase immiscible CO_2 injection experiment in the mixed-wet reservoir rock at high temperature and pressure conditions. The dashed line represents the micro-CT scanner enclosure. A cross-section of the coreholder is shown to illustrate how the sample is connected to the flow lines. Experimental conditions are 8 MPa and 60 °C.

Table 4

Details of the flooding experiment. The capillary number between the different fluids was calculated using $Ca = \mu q / \sigma$ where σ is the interfacial tension, μ is the viscosity of the displacing (injected) fluid and q is the Darcy velocity. μ and σ are shown in Table 3, while q is calculated by dividing the flow rate by the cross-sectional area of the sample (29.22 mm^2). Subscripts w, g and o stand for water, gas and oil phases respectively. Two pore volumes of fluid were injected in the sample during each flooding sequence.

Injection Sequence	Flow rate (mL/min)	Capillary number [Ca]
First waterflooding [WF1]	0.005	$Ca_{[wo]} = 6.29 \times 10^{-8}$
Gas Injection [GI]	0.005	$Ca_{[gw]} = 2.12 \times 10^{-9}$ $Ca_{[go]} = 6.73 \times 10^{-9}$
Second waterflooding [WF2]	0.005	$Ca_{[wg]} = 4.30 \times 10^{-8}$ $Ca_{[wo]} = 6.29 \times 10^{-8}$

2.4. Image acquisition and segmentation

After each injection, the fluids within the rock were allowed to reach equilibrium for two hours and then the ZEISS Xradia 510 Versa micro-CT scanner was used to acquire three-dimensional images of the sample. A photon energy and power of 80 keV and 7 W were applied respectively at the X-ray source, with a 360° sample rotation. No physical filter (air) was used between the source and sample. Scans with two resolutions were acquired every time: (i) four 3.57 μm per voxel scans were taken at different locations to construct an image of the whole sample, see Fig. 2; and (ii) a zoomed in 1.82 μm per voxel scan was taken close to the centre of the sample. For the low-resolution scans at 3.57 μm /voxel, a flat panel extension was employed at the detector to maximize the field of view, with an exposure time of 2 s and a total of 3201 projections. For the high-resolution scans at 1.82 μm /voxel, a 4X objective was employed with an exposure time of 4 s and 5001 projections. The high-resolution scan was

acquired to accurately characterize resolution sensitive properties including fluid-fluid/fluid-solid specific interfacial areas, fluid-fluid interfacial curvatures, connectivity and contact angles.

The 2D projections of the sample were then reconstructed at different angles to obtain raw 3D images of the rock and fluids within it after each injection, see Fig. 3. Two segmentation methods were employed to segment the raw images: (i) seeded watershed algorithm (Jones et al., 2005); and (ii) machine learning-based trainable WEKA (Arganda-Carreras et al., 2017). The seeded watershed algorithm was used to segment the lower resolution images, 3.57 μm /voxel, of the whole sample, while the higher resolution images, 1.82 μm /voxel, were segmented using WEKA. Both segmentation methods provide accurate phase identification and can overcome misclassifications at the fluid-fluid/fluid-solid boundaries caused by the partial volume effect (Kaynig et al., 2010; Rudyanto et al., 2014; Brown et al., 2014; Garfi et al., 2020). However, WEKA is better at preserving the shape of the interface between the phases, facilitating more accurate characterization of flow properties (Alhammadi et al., 2017). Nevertheless, it is very CPU intensive, and hence it was not possible to apply it to the large 3.57 μm /voxel images of the whole sample.

Prior to segmenting the large 3.57 μm /voxel resolution images they were filtered using a non-local means filter to reduce the image noise, allowing for a more accurate subsequent watershed segmentation (Buades et al., 2008). Watershed segmentation consisted of two steps: (i) seeding, where the homogeneous regions of each phase (high certainty regions) were flooded with seeds; and (ii) growing, where the implemented seeds were grown proportionally until they reached a boundary, where two phases meet. At the boundary, the algorithm detects the intensity gradient of each phase in the raw image and classifies the voxels at the boundary accordingly. On the other hand, no filtering was applied to the high-resolution images, 1.82 μm /voxel, prior to segmenting them to avoid averaging of the grey-scale values at the fluid-fluid/fluid-solid contacts which might introduce artificial artefacts to their interfaces.

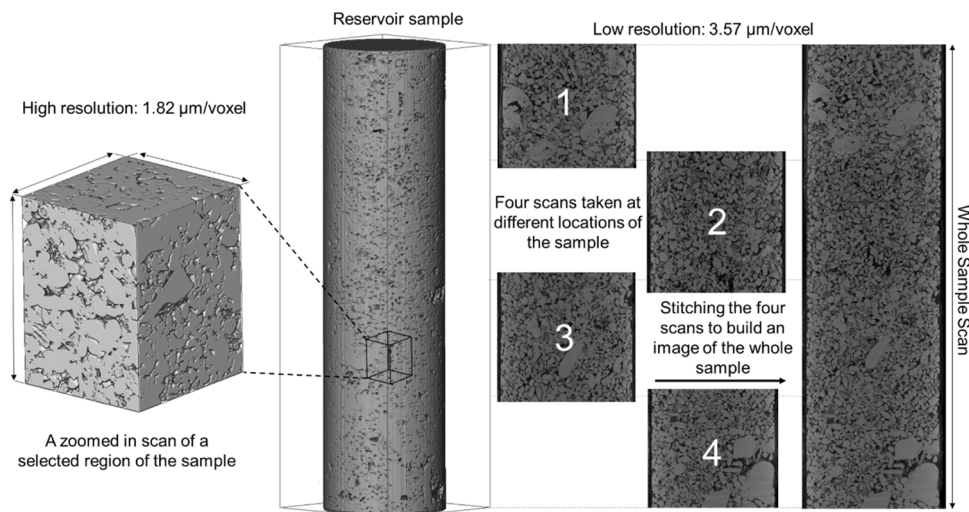


Fig. 2. A schematic showing the location of the four low-resolution scans, $3.57 \mu\text{m}$ voxel size, taken to construct an image of the whole sample ($1157 \times 1146 \times 5517$ voxels), and the high-resolution scan, $1.82 \mu\text{m}$ voxel size, taken almost at the centre of the sample ($1381 \times 1404 \times 1689$ voxels).

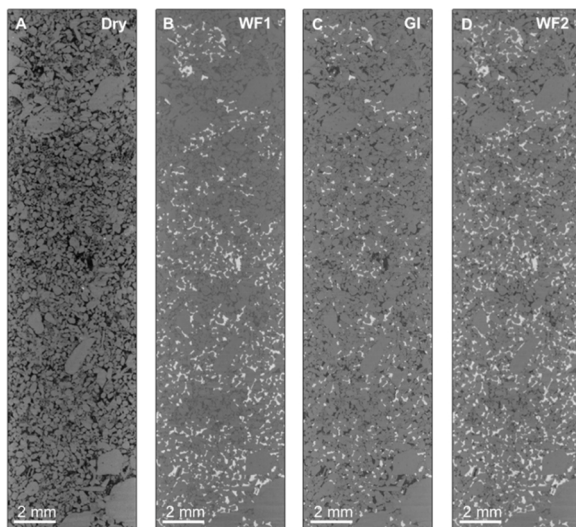


Fig. 3. A series of raw images with a $3.57 \mu\text{m}$ /voxel resolution of the whole sample after each injection sequence. From left to right: (i) A dry scan of the rock; (ii) After first waterflooding (WF1); (iii) After gas injection (GI); and (iv) after second waterflooding (WF2). In the dry scan, the rock is shown in grey and the pore space is in black. In the wet images, water is white, rock is light grey, oil is dark grey, and gas is black.

(Alhammadi et al., 2018). The trainable WEKA classifier was trained by manually assigning voxels to the oil, rock, brine and gas phases in the raw images. The classifier uses a fast-random algorithm alongside selected mean and variance texture filters. After training the classifier, it was applied to the raw images to segment the different phases. Fig. 4 shows raw and segmented pore-scale images of the high-resolution scans.

2.5. Gas layers

In this section, we describe a curvature analysis that allows us to investigate whether spreading gas (CO_2) layers can be present in the pore spaces of the rock or not. Given that CO_2 is predicted to be the intermediate phase, it may spread in pore-sized (microns) layers separating oil in the corner and water in the centre of the pore space. The existence of CO_2 in layers will have an impact on its relative

permeability and thence its flow conductance in the reservoir.

2.5.1. Curvature analysis

There are two necessary criteria for spreading gas layers to form in an oil-wet system with an oil-gas-water wettability order. (i) The first is that the gas spreading coefficient ($C_{sg} = \sigma_{ow} - \sigma_{gw} - \sigma_{go}$, where o , w and g label oil, water and gas, CO_2 , respectively) must be close to zero. From Table S1, we find that $C_{sg} = -2 \text{ mN/m}$ for near-miscible conditions. This value is sufficiently close to zero to allow layers to form (Alhosani et al., 2020b). However, for immiscible flooding $C_{sg} = -19.5 \text{ mN/m}$, Table 3, which prohibits the formation of layers. (ii) The second criterion is that the values of gas-oil and gas-water interfacial curvatures must satisfy the following inequality, as illustrated in Fig. 5:

$$\kappa_{mgo} > \kappa_{mgw} \quad (1)$$

where κ_m is the mean curvature of the fluid-fluid interface. In Fig. 5, the curvature of the fluid-fluid interface is assumed to be the inverse of the radius of curvature, while the other radius – out of the plane of the figure – is much larger. The mean curvature can be related to the capillary pressure through the Young-Laplace equation:

$$P_c = 2\sigma\kappa_m \quad (2)$$

where σ is the interfacial tension between two phases. Hence, Eq. (1) can be written as an inequality involving P_{cgw} and P_{cgo} , the capillary pressures between gas-water and gas-oil phases respectively:

$$P_{cgo} > \frac{\sigma_{go}}{\sigma_{gw}} P_{cgw} \quad (3)$$

Using representative interfacial tension values, Tables 3 and 1S, Eq. (3) can be plotted as shown in Fig. 5. The next section provides details on how the curvature is estimated. Fig. 5 (right) indicates that if the ratio of P_{cgo} to P_{cgw} falls above the critical line, the black line spanning the diagram, gas layers can form in a three-phase rock system with a wettability order of oil-gas-water. Furthermore, the interfacial tension between the fluids change when switching from immiscible to near-miscible gas-oil conditions, hence, by plotting Eq. (3) at the two conditions, we observe that the critical line is much steeper at immiscible conditions compared to the near-miscible case indicating again that it is much harder for gas layers to form at immiscible conditions.

The overall conclusion of this analysis is that gas layers will not form under immiscible conditions but may be seen under the near-miscible conditions studied in our experiments.

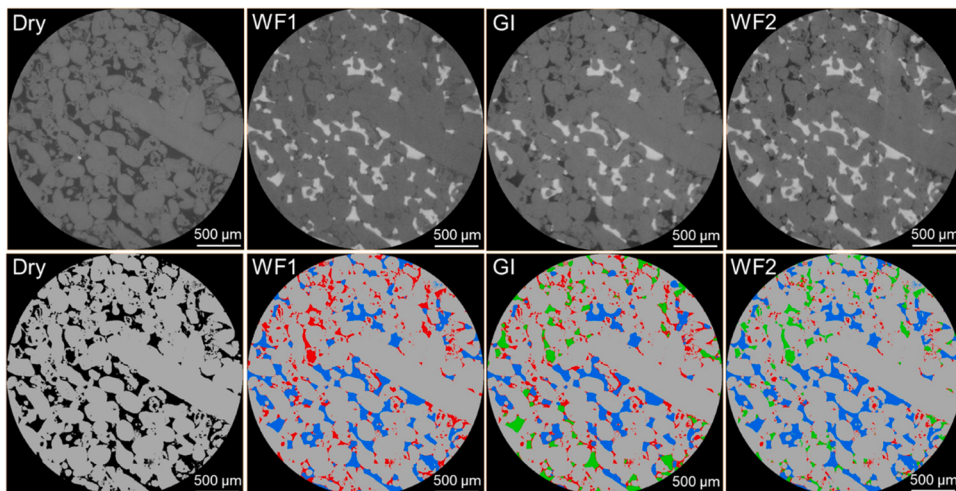


Fig. 4. Raw (top row) and segmented (bottom row) pore-scale images of the higher resolution scans, 1.82 μm voxel size, showing (top row, from left to right) raw images of: (i) a dry scan of the rock; (ii) first waterflooding (WF1); (iii) gas injection (GI); and (iv) second waterflooding (WF2). The bottom row shows the segmentation of the images in the top row, segmented using WEKA segmentation method. In the raw images, gas is shown in black, rock in light grey, oil in dark grey and water in white. In the segmented images, gas is shown in green, rock in grey, oil in red and water in blue.

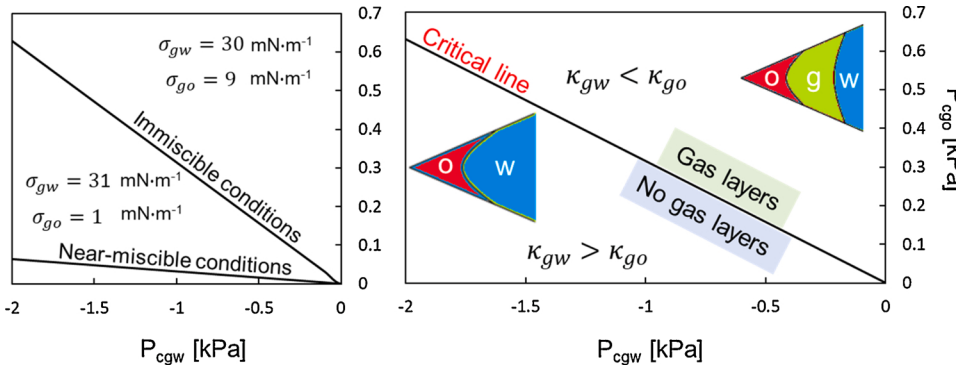


Fig. 5. A graphical representation of Eq. (3) that helps determine the likely formation of gas layers in an oil-wet system with a wettability order of oil-gas-water depending on the microscopic gas-water and gas-oil capillary pressures. (right) The graph illustrates that if the ratio of P_{cgo} to P_{cgw} falls above the critical line, gas layers will form as a much lower P_{cgo} will be needed to squeeze out the gas-oil interface ($\kappa_{gw} > \kappa_{go}$) and vice versa. (left) The critical line is less steep at near-miscible conditions (Alhosani et al., 2020b) compared to immiscible conditions and therefore it is more likely for gas layers to form at near-miscible conditions for the same gas-oil capillary pressure.

2.5.2. Capillary pressure measurement

To quantify the capillary pressures between oil, water and CO₂, we adopted the curvature-based capillary pressure measurement approach pioneered by Armstrong et al. (2012). In this approach, the Young-Laplace equation, (2), is used to link the measured interfacial curvature between each fluid pair to their capillary pressure. The curvatures of oil-water, gas-water and gas-oil interfaces were measured from the segmented pore-scale images using a method previously presented in the literature (Armstrong et al., 2012; Andrew et al., 2014a; Li et al., 2018; Lin et al., 2018, 2019; Akai et al., 2019). To measure the curvature of the interfaces, each fluid-fluid interface was first extracted using a marching cube algorithm. The extracted interfaces were then smoothed, kernel size = 5, in the direction of the less wetting phase, water in the case of gas-water and oil-water interfaces, and gas in the case of a gas-oil interface. After smoothing the interface, it was modelled using a quadratic form ($ax^2 + by^2 + cz^2 + 2exy + 2fyz + 2gzx + 2lx + 2my + d = 0$). The eigenvalues and eigenvectors of this quadratic form corresponded to the principal curvatures of the interface and their directions, respectively. The mean of the principal curvatures was then taken and substituted in the Young-Laplace equation, (2), alongside the interfacial tension values to obtain the microscopic gas-water, gas-oil and oil-water capillary pressures.

3. Results and discussion

In this section, we quantify pore-scale properties that are relevant to carbon dioxide storage and oil recovery in our immiscible oil-wet experiment and compare the results to that of Alhosani et al. (2020b) for near-miscible conditions. First, in section 3.1, we start by characterizing the rock surface wettability at immiscible and near-miscible

conditions by: (i) measuring the geometric contact angle between the three fluid phases; and (ii) quantifying the pore occupancy of each phase. This allows us to verify the anticipated order of wettabilities in the two systems – oil-gas-water from most to least wetting. Next, we qualitatively and quantitatively confirm the presence of gas layers at near-miscible conditions and their absence at immiscible conditions by examining the fluid configurations and connectivity *in situ*, as well as measuring the Euler characteristic in Section 3.2. In Section 3.3, we use the capillary pressure measurements to conduct the curvature analysis detailed in section 2.5.1 to quantitatively show that the necessary criteria for gas to spread in layers are fulfilled at near-miscible conditions in contrast to immiscible conditions. Finally, in sections 3.4 and 3.5, for immiscible and near-miscible conditions, we (i) measure the specific interfacial areas between the fluids and the fluids and rock; (ii) quantify the saturations of water, oil and CO₂ after each injection step; and (iii) examine the trapping mechanisms for both cases. We synthesize the results in Section 3.6 by discussing the implications of these results on CO₂ storage and oil recovery under each CO₂ injection condition (immiscible or near-miscible) in CCS-EOR projects.

3.1. Wettability characterization

3.1.1. Contact angles

The geometric contact angle between the fluids was measured after gas injection (GI) on a segmented high-resolution, 1.82 $\mu\text{m}/\text{voxel}$, sub-volume ($1,500 \times 1,500 \times 400 \mu\text{m}^3$) of the pore space using the automated algorithm developed by AlRatrou et al. (2017) at immiscible and near-miscible conditions. The distribution of the effective contact angles between oil-water (measured through water), CO₂-water (measured through water), and CO₂-oil (measured through oil) are shown in Fig. 6.

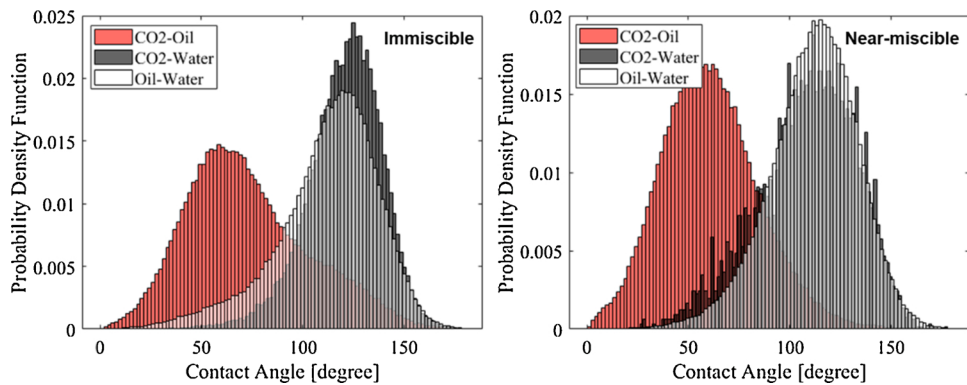


Fig. 6. Normalized histograms of the measured *in situ* contact angles between CO₂-water, oil-water and CO₂-oil in the aged rock at (left) immiscible conditions and (right) near-miscible conditions. The contact angles were measured through the denser phase: water in the case of oil-water and CO₂-water contact angles, and oil in the case of the CO₂-oil contact angle. The contact angles were measured using the automated method developed by AlRatrou et al. (2017).

By convention, the contact angle between oil and water is considered the direct measure of the wettability of the surface (Andrew et al., 2014b; Khishvand et al., 2016; Blunt, 2017). Fig. 6 depicts that both the immiscible and near-miscible systems are oil-wet systems with an average oil-water contact angle of 118° and 112° respectively. The reservoir rocks used in the two experiments were aged dynamically in the same coreholder; however, in the immiscible experiment the rock was left to statically age for eight months, while it was statically aged for four months only in the near-miscible experiment. This has resulted in the slightly more oil-wet surface in the immiscible experiment as shown by the higher average oil-water contact angle. From Fig. 6, it is also evident that the CO₂-water contact angle is higher than 90° in both immiscible and near-miscible experiments indicating that water is less wetting than CO₂ in the pore space, while the CO₂-oil contact angle is below 90° indicating that oil is more wetting than CO₂. This shows that the wettability order under both oil-wet immiscible and near-miscible conditions is oil-gas-water from most to least wetting. The oil-water contact angle was also measured after the first waterflooding (WF1) and the second waterflooding (WF2) for the immiscible system and showed a consistent distribution throughout the injection sequence, which confirms that there was no wettability alteration during the flooding experiment: see Fig. S1 in the supplementary material.

In equilibrium, the Bartell-Osterhof relationship can be used to determine the CO₂-water contact angle from the oil-water and CO₂-oil angles and interfacial tensions (Bartell and Osterhof, 1927; Blunt, 2001):

$$\sigma_{gw}\cos\theta_{gw} = \sigma_{go}\cos\theta_{go} + \sigma_{ow}\cos\theta_{ow} \quad (4)$$

The predicted values of θ_{gw} are shown in Table 5 together with the measured values, using the interfacial tensions in Tables 3 and S1. In the near-miscible case, since the gas-oil interfacial tension is low and the gas-water and oil-water interfacial tensions are similar, then from Eq. (4) we predict that $\theta_{gw} \approx \theta_{ow}$, which is consistent with our measurements.

On the other hand, we measure a larger gas-water contact angle under immiscible conditions than predicted from Eq. (4). The reason for this discrepancy is that the Bartell-Osterhof relationship holds at one location in equilibrium, while we are measuring the contact angles in

different locations for different fluid pairs in a rock where the contact angle varies spatially. It appears that CO₂ (the gas phase) occupies the more oil-wet pores: the larger oil-wet pores are filled with water during waterflooding. During gas injection, CO₂ preferentially displaces water from the most oil-wet (and hence gas-wet) pores, since this is most favoured in an imbibition displacement. On the other hand, water remains in more water-wet pores. Hence for the gas-water angle the values are biased towards larger values of contact angle.

3.1.2. Pore occupancy

The pore occupancy of each fluid phase inside the rock was quantified at immiscible and near-miscible conditions using the approach developed by Scanziani et al. (2018b). In this approach, using a dry scan of the sample, the pore sizes are found by fitting the largest possible sphere in each pore, the diameter of that sphere is the pore diameter (Dong and Blunt, 2009; Raeini et al., 2017). The extracted spheres are then mapped on the wet pore-scale images and the occupancy of each phase is determined based on the grey-scale value of the phase occupying that sphere. Pore occupancy was quantified on pore-scale images of the whole sample (4,000 × 4,000 × 20,000 μm³). The pore occupancies after the first waterflooding (WF1), gas injection (GI) and second waterflooding (WF2) at immiscible and near-miscible conditions are shown in Fig. 7. As expected for the oil-wet rocks in the immiscible and near-miscible experiments, the injection of water during WF1 displaces oil, the wetting phase, from the larger pores confining it into smaller ones; water resides in the biggest pores, Fig. 7a and d.

The pore occupancies after GI and WF2 at both conditions confirm that the wettability order is oil-gas-water from most to least wetting. As shown in Fig. 7, water is the most non-wetting phase with a tendency to occupy the largest pores, CO₂ is the intermediate-wet phase occupying the medium-sized pores, while oil is the most wetting phase occupying the smallest pores.

The injection of CO₂ principally displaces water in both cases: this is because the CO₂ is wetting to water, see Table 5, and hence this represents a favourable imbibition process. CO₂ will preferentially fill the more oil-wet pores (which from Eq. 4 will be more gas-wet); this is evident from the contact angle distributions after gas injection shown in Fig. 6. There is also some displacement of oil, which is a less favoured drainage process, as gas is non-wetting to oil. More oil is displaced at near-miscible conditions, see Figs. 7b and e. This is attributed to the low gas-oil interfacial tension (1 mN/m) compared to immiscible conditions (9 mN/m) which results in a lower gas-oil capillary pressure; see section 3.3 for capillary pressure values. A low gas-oil capillary entry pressure allows CO₂ to invade a larger fraction of the smaller pores resulting in an efficient displacement of oil by gas at near-miscible conditions. Moreover, during gas injection (GI) at immiscible and near-miscible conditions, water gets trapped in the centres of the pore space as disconnected

Table 5

Measured oil-water (θ_{ow}), gas-oil (θ_{go}), and gas-water (θ_{gw}) contact angles after gas injection (GI) at immiscible and near-miscible conditions together with the predicted θ_{gw} using the Bartell-Osterhof relationship, Eq (4), using the mean values. The measured mean values and standard deviations are of the contact angle distributions shown in Fig. 6.

Miscibility state	Measured θ_{ow}	Measured θ_{go}	Measured θ_{gw}	Predicted θ_{gw}
Near-miscible	112 ± 21°	67 ± 22°	108 ± 18°	110°
Immiscible	118 ± 25°	60 ± 24°	124 ± 24°	103°

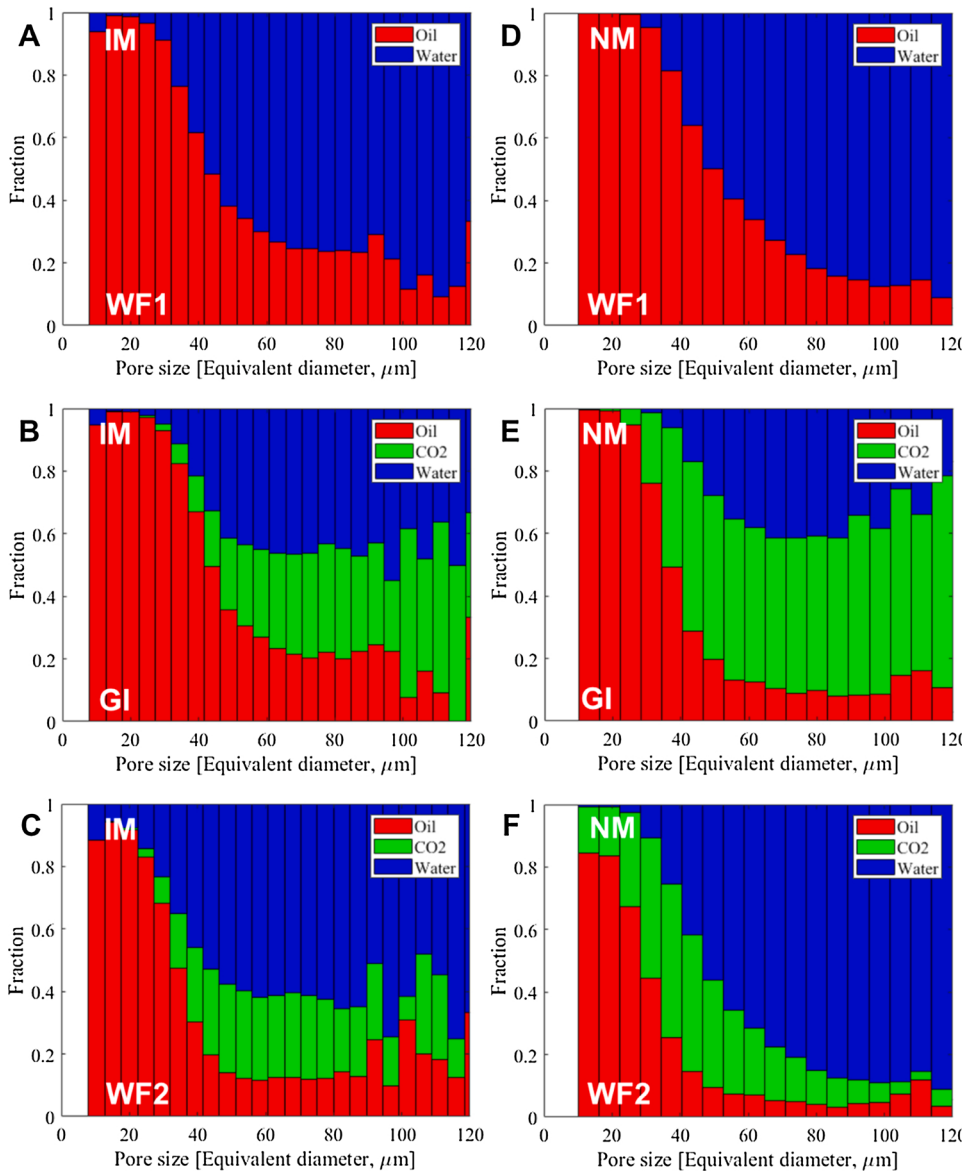


Fig. 7. Coloured bar charts showing the pore occupancy of each fluid phase in the pore space after first waterflooding [WF1] at (A) immiscible conditions and (D) near-miscible conditions, after gas injection [GI] at (B) immiscible conditions and (E) near-miscible conditions, and after second waterflooding [WF2] at (C) immiscible conditions and (F) near-miscible conditions. Pore occupancy is defined as the phase occupying the centre of the pore – this phase will also have the largest volume in the pore. Pore occupancy was quantified on pore-scale images of the whole sample ($4000 \times 4000 \times 20,000 \mu\text{m}^3$). Oil is shown in red, water in blue and gas, CO₂, in green.

ganglia since it is the most non-wetting phase, as described in the next section.

During the second waterflooding (WF2), at near-miscible conditions, water invades the centres of the larger pores confining CO₂ and oil to smaller sized pores: CO₂ is forced to occupy smaller pores than those filled during GI, see Fig. 7f. On the other hand, during second waterflooding (WF2) at immiscible conditions, the injection of water causes CO₂ to displace more oil out of the intermediate sized pores, shuffling it into some of the larger pores by a double displacement process (van Dijke et al., 2001b), where water displaces gas that displaces oil: this is a double drainage event (Oren et al., 1992), see Fig. 7c. This behaviour is explained further in Section 3.2 when we analyse gas layers.

3.2. Fluid configurations and connectivity

Fig. 8 shows example 2D and 3D images of a trapped water ganglion in a single pore during gas injection (GI) at both immiscible and near-miscible conditions. We observe that at near-miscible conditions, CO₂, the intermediate-wet phase, spreads in layers surrounding water, the most non-wetting phase. CO₂ exists in sheet-like layer structures at near-miscible conditions as shown by Alhosani et al. (2020b). However, no

evidence was found of oil residing in the corners when CO₂ invaded the pore (at this resolution); CO₂ layers are not sandwiched between oil in the corners and water in the centre. Because of the lower gas-oil interfacial tension (1 mN/m) compared to the gas-water interfacial tension (31 mN/m), Table S1, at near-miscible conditions, the gas front efficiently displaces all the oil in the corners, leaving water stranded in the centres of the pore space. CO₂ layers do not appear to coexist with oil in the same pore at near-miscible conditions. A similar behaviour was observed by Alhosani et al. (2019) in a water-wet system, where the injection of CO₂, the most non-wetting phase, at near-miscible conditions displaced all the oil, the intermediate-wet phase, in the pore space preventing it from spreading in layers.

At immiscible conditions however, CO₂ does not form layers but instead exists as disconnected ganglia in the pore space, see Fig. 8. This is consistent with the very negative gas spreading coefficient in this case, see Table 3 and Fig. 5. This means that CO₂, water and oil cannot reside in the same pore under immiscible conditions. CO₂ can either be present with water or oil in the same pore, occupying the corners of the pore in the case of water, and the centres in the case of oil. This limitation means that during water injection, one of the principal displacement processes is likely to be double drainage where water displaces CO₂ which then

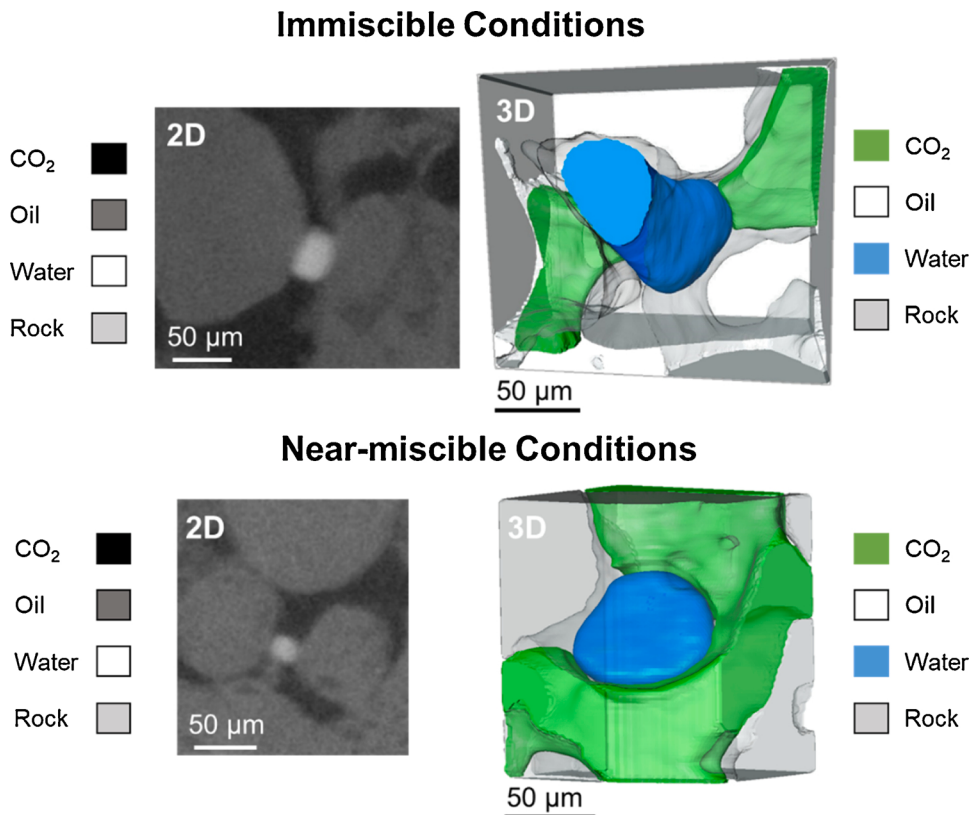


Fig. 8. Example two-dimensional raw images and three-dimensional segmented images of a trapped water ganglion in a single pore after gas injection (GI) at immiscible and near-miscible conditions. CO₂ spreads in layers at near-miscible conditions, while it exists as disconnected clusters at immiscible conditions. The size of the 3D subvolumes shown at immiscible and near-miscible conditions are 185 × 209 × 121 μm³ and 109 × 134 × 152 μm³ respectively. The pore-scale images were acquired by X-ray micro-tomography at a resolution of 1.82 μm per voxel.

displaces oil in some of the larger pores, as discussed in the context of the pore occupancy, Fig. 7c. Unlike near-miscible conditions, CO₂ does not displace all the oil it contacts due to the higher gas-oil interfacial tension (9 mN/m), Table 3.

To examine the connectivity of the water and CO₂ phases in the macro pore space, we plotted 3D coloured volume maps identifying the size of each disconnected phase cluster – a large range of colours represents a poorly connected phase, while a narrow colour distribution indicates better connectivity. The connectivity of the water and CO₂

phases after gas injection (GI) and second waterflooding (WF2) are shown in Fig. 9 at immiscible and near-miscible conditions. In general, although not very well connected, the connectivity of CO₂ is slightly improved at near-miscible conditions. This is attributed to the existence of CO₂ in sheet-like layers at near-miscible conditions, while CO₂ forms disconnected ganglia and no layers at immiscible conditions, see Fig. 8. Nevertheless, at immiscible conditions, the CO₂ has a tendency to occupy some of the larger pores, Fig. 7, so that, for the same saturation, it is likely to have a larger flow conductance than under near-miscible

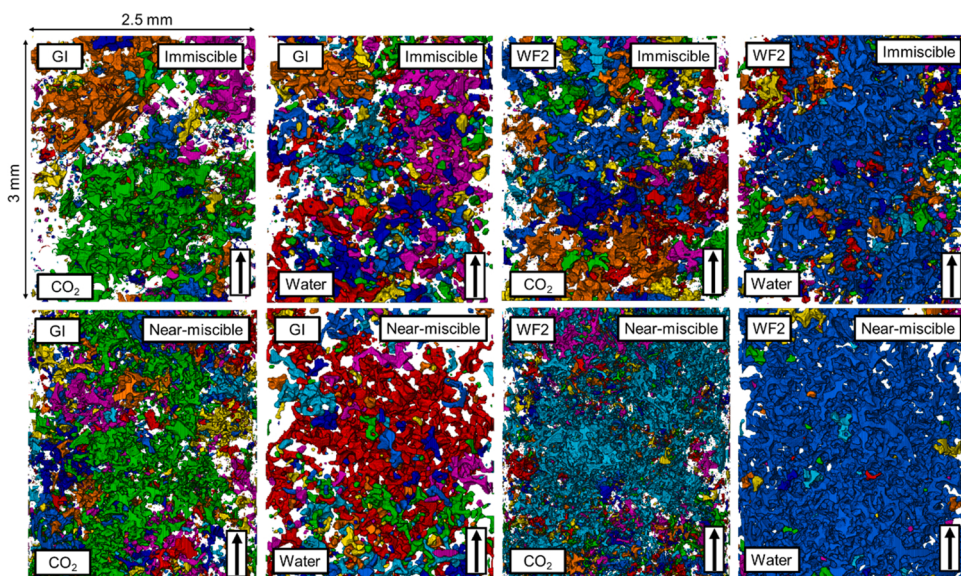


Fig. 9. Three-dimensional maps showing the connectivity of water and CO₂ phases during gas injection (GI) and second waterflooding (WF2) at immiscible and near-miscible conditions. The colours indicate discrete clusters of each phase. Each subvolume is of 2500 × 2500 × 3000 μm³ size and 1.82 μm/voxel size. The vertical arrow points in the flow direction.

conditions. The CO₂ follows a tortuous path through the pore space in both cases, however.

There is more water trapping (water is highly disconnected) during gas injection (GI) at immiscible conditions compared to near-miscible conditions. This is because, since CO₂ cannot form layers, both phases essentially compete to occupy some of the larger and medium-sized pores, blocking each other's flow. During the second waterflooding (WF2), water forms a connected path through the larger pores at both conditions. While not shown in Fig. 9, oil exists in highly connected thick wetting layers close to the rock surface: the oil wetting layer becomes thinner as more oil gets produced throughout the flooding experiment.

To quantitatively assess the connectivity of oil, water and CO₂, we measured the Euler characteristic which quantifies the topology of the fluid phases within the pore space (Herring et al., 2013, 2015; Mecke and Wagner, 1991; Vogel and Kretzschmar, 1996; Vogel, 2002), see Table 6. A large negative Euler characteristic indicates that the fluid phase is interconnected with many redundant loops, while a phase that is trapped into many discrete ganglia exhibits a large positive Euler number (Herring et al., 2019). The fluid phases in the high-resolution, 1.82 μm/voxel, subvolumes, size 2,500 × 2,500 × 3,000 μm³, were isolated and the small features (below 100 voxels) were filtered out prior to measuring the Euler characteristic of each phase, consistent with previous work (Herring et al., 2019).

The results in Table 6 confirm the qualitative observations made based on Fig. 9. Water has a positive Euler number after gas injection at both immiscible and near-miscible conditions confirming its existence in disconnected clusters in the centre of the pores, see Fig. 8, consistent with water being the most non-wetting phase. The water phase Euler characteristic decreases, as expected, after waterflooding. Under immiscible conditions water is still trapped in some of the larger pores giving a characteristic that remains positive, as evident in Fig. 9. After gas injection at both miscibility conditions, CO₂ has a smaller negative Euler number compared to oil which is well-connected in wetting layers. The CO₂ Euler number is larger at near-miscible conditions, -634 mm⁻³, compared to immiscible conditions, -102 mm⁻³, after WF2, confirming the enhanced CO₂ connectivity at near-miscible conditions due to its existence in spreading layers.

3.3. Capillary pressure and curvature analysis

Using the curvature-based approach described in Section 2.5.2, the capillary pressure between the fluids was measured after each injection step at immiscible and near-miscible conditions, see Fig. 10. The capillary pressure measurements were performed on high-resolution, 1.82 μm/voxel, subvolumes of size 2,500 × 2,500 × 3,000 μm³. The saturations, see Section 3.5, only consider phases in the resolvable macro pore space.

At both immiscible and near-miscible conditions, the capillary pressure between oil and water was negative, indicating that the pressure in the water phase is higher than oil, which is a characteristic of predominantly oil-wet media. The oil-water capillary pressure is more negative at near-miscible conditions, ranging from -1.3 kPa to -2.4 kPa,

compared to immiscible conditions, ranging from -0.5 kPa to -1 kPa, Fig. 10. This is partially attributed to the higher oil-water interfacial tension in the near-miscible experiment (30 mN/m) compared to the immiscible experiment (21 mN/m), see Tables 3 and S1. In addition, under near-miscible conditions, as shown in Fig. 7, oil tends to reside in smaller pores, which again would give a larger (more negative) capillary pressure. The fact that the average oil-water contact angles are higher in the immiscible case does not result in a more negative capillary pressure. As expected, the oil-water capillary pressure decreased with increasing water saturation at near-miscible conditions. However, in the immiscible experiment, the oil-water capillary pressure is more negative during gas injection (GI) at a lower water saturation. At the beginning of gas injection, after the first waterflood, the capillary pressure is likely to be large and negative, as the water displaces oil from increasingly small and oil-wet regions of the pore space. During gas injection, since the principal displacement is gas displacing water as an imbibition process, with a lower gas pressure than water, then P_{cow} can continue to have a large negative value while the gas pressure increases before gas is able to displace oil. During waterflooding, Fig. 7c, double displacement moves oil into larger pores, as discussed above, with a less negative capillary pressure.

The measured gas-water capillary pressure ranged from -0.5 kPa to -2.5 kPa at both immiscible and near-miscible conditions. A negative gas-water capillary pressure indicates that gas is more wetting to the rock surface than water. This confirms the reported wettability order of oil-gas-water from most to least wetting in Section 3.1. Under immiscible conditions, we again see that the capillary pressure is less negative (higher) during WF2. Again, this is due to double displacement, and the fact that water displaces gas from the larger pores, see Fig. 7c. Note that this leads to a trend of capillary pressure with saturation which is counter-intuitive: an increase with increasing water saturation. This shows that in three-phase flow the capillary pressure is a function of both saturation and displacement path (van Dijke et al., 2001a; van Dijke and Sorbie, 2003; van Dijke et al., 2004).

The gas-oil capillary pressure was positive at both immiscible and near-miscible conditions, indicating that oil is more wetting than gas, Table 3. As expected, the capillary pressure between gas and oil is higher at immiscible conditions (0.26 kPa to 0.38 kPa) compared to near-miscible conditions (0.04 kPa to 0.08 kPa) due to the higher gas-oil interfacial tension, see Tables 3 and S1.

The gas-water and gas-oil capillary pressure values in Fig. 10 were used to conduct the curvature analysis described in Section 2.5.1, see Fig. 5, to quantitatively confirm that the gas layer spreading criteria are met at near-miscible conditions and that gas does not form layers at immiscible conditions. The results are shown in Fig. 11. At immiscible conditions, during gas injection (GI), the ratio of P_{cg0} to P_{cgw} falls below the critical line, suggesting that gas layers do not form, see Fig. 11 (left). During WF2, the curvature analysis indicates that layers are possible, but the large negative spreading coefficient of -19.5 mN/m, Table 3, in this case prevents their formation. In contrast, at near-miscible conditions, the P_{cg0} to P_{cgw} ratio lies above the critical line suggesting the formation of stable gas layers, see Fig. 11 (right). The formation of gas layers is also supported by a gas spreading coefficient close to zero at near-miscible conditions ($C_{sg} = -2$ mN/m, Table S1).

The existence of CO₂ in layers at near-miscible conditions substantially impedes its movement in the reservoir. While these layers maintain connectivity, they have low relative permeability (low flow conductivity) in the pore space of the rock. This was shown by Alhosani et al. (2020b) who computed the relative permeability of these layers on pore-space images. On the other hand, we predict a higher CO₂ relative permeability at immiscible conditions, where CO₂ occupies some of the larger pores, Fig. 7, and exists in blobby structures; its flow is not confined to movement in layers.

Table 6

Euler characteristic of water, CO₂ and oil measured after gas injection [GI] and second waterflooding [WF2] at immiscible and near-miscible conditions. The Euler characteristic number was measured on high resolution images, 1.82 μm/voxel, and normalized to the total volume in both cases.

Miscibility state	Normalized Euler Characteristic (mm ⁻³)					
	Gas Injection [GI]			Second waterflooding [WF2]		
	Water	CO ₂	Oil	Water	CO ₂	Oil
Immiscible	125	-504	-5055	21	-102	-17298
Near-miscible	90	-499	-17851	-2318	-634	-24027

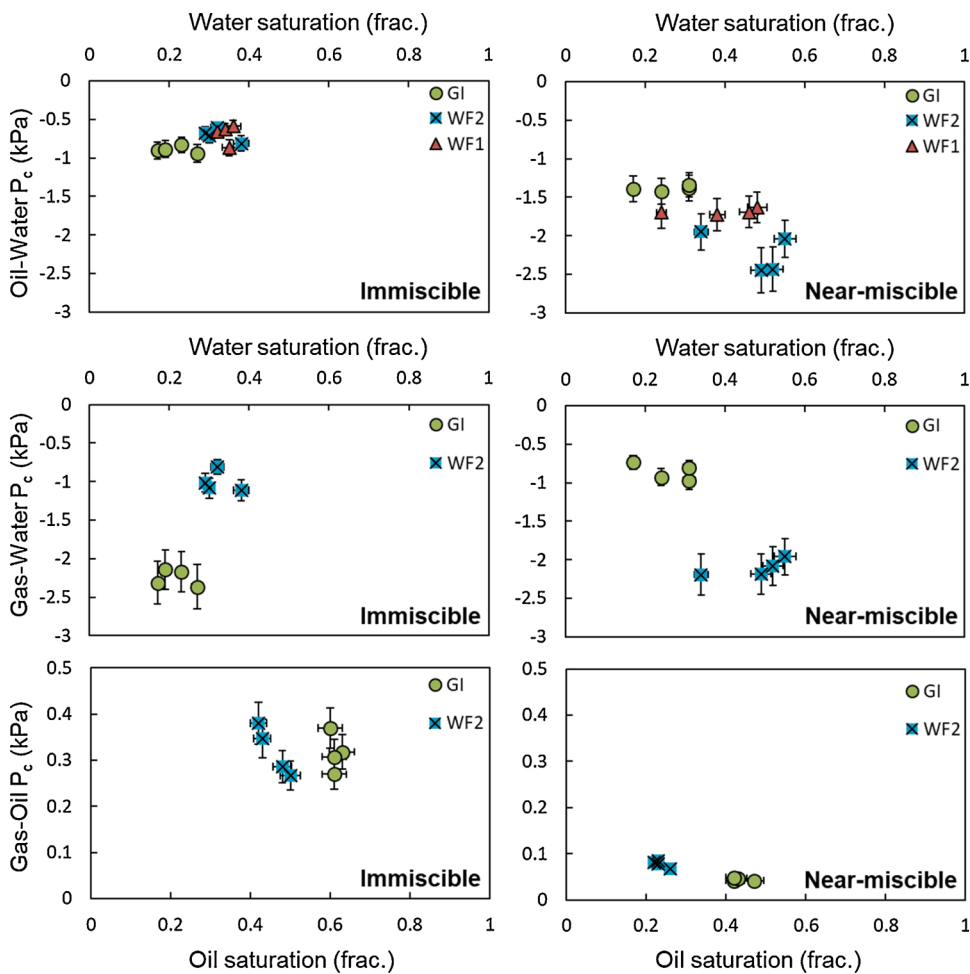


Fig. 10. Capillary pressures estimated from the average curvature of the fluid-fluid interfaces plotted as a function of water saturation in the case of oil-water and gas-water capillary pressures and as a function of oil saturation in the case of the gas-oil capillary pressure. Capillary pressure measurements after first waterflooding (WF1), gas injection (GI) and second waterflooding (WF2) are shown (left column) at immiscible conditions and (right column) at near-miscible conditions. Error bars indicate the uncertainty in the measurements.

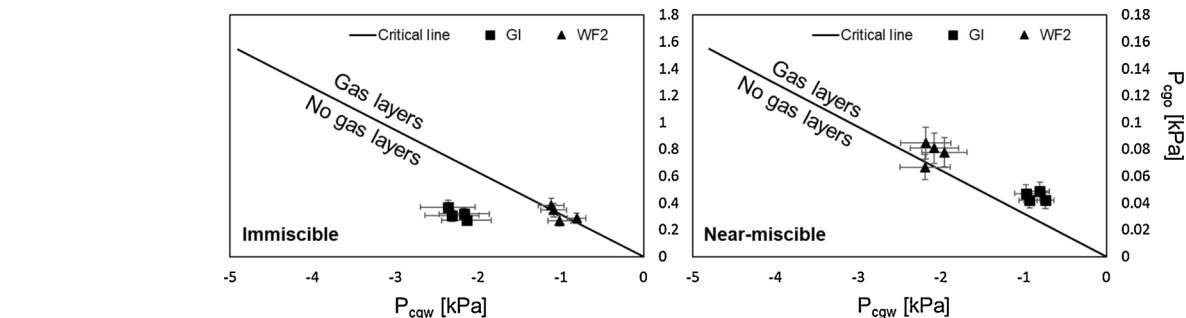


Fig. 11. Curvature gas layer analysis conducted at (left) immiscible conditions and (right) near-miscible conditions. The graphs illustrate that under immiscible conditions gas layers do not form, while gas can form layers under near-miscible conditions. Error bars indicate the uncertainty in the measurements.

3.4. Interfacial area

We also quantified the specific interfacial areas – area per unit volume (total volume of rock and pore space) – between each fluid pair and between the fluids and the rock surface (solid) at both conditions, see Fig. 12. From Fig. 12a and b, we observe that the CO₂-water interfacial area is higher at near-miscible conditions compared to immiscible conditions: this is caused by the presence of CO₂ layers which surround the water phase increasing their direct contact in the pore space. Moreover, the CO₂-water interfacial area increases during WF2 at both conditions since more water is present, allowing more contact between the two phases. As expected, the oil-water interfacial area decreases as oil is produced under both immiscible and near-miscible

conditions. This also explains why the oil-solid interfacial area decreases throughout the flooding experiment, see Fig. 12c and d.

The CO₂-oil interfacial area is higher at immiscible conditions compared to near-miscible conditions (Fig. 12a and b): this is an initially surprising result as one would expect a higher gas-oil interfacial area at near-miscible conditions given the low gas-oil interfacial tension which makes a gas-oil interface more energetically favourable to form in the pore space, combined with the presence of gas layers. This behaviour, however, can be ascribed to the low gas-oil capillary entry pressure at near-miscible conditions: gas will almost always have sufficient pressure to displace oil efficiently out of the pores minimizing their direct contact in the pore space. This is similar to the efficient displacement of oil that was also observed in a near-miscible water-wet system (Alhosani et al.,

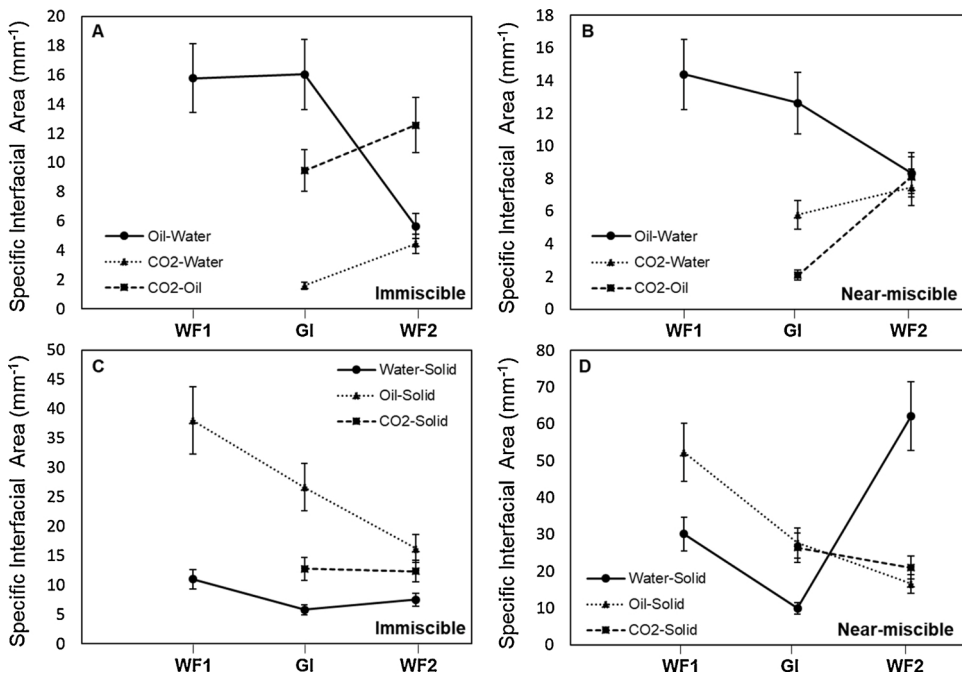


Fig. 12. Specific interfacial area measurements between each fluid pair in the pore space at (A) immiscible conditions and (B) near-miscible conditions, and between the fluids and the rock surface (solid) at (C) immiscible conditions and (D) near-miscible conditions. The specific area is calculated on extracted fluid-fluid and fluid-solid interfaces from segmented images. The measurements were performed on high-resolution, 1.82 μm/voxel, subvolumes of size 2500 × 2500 × 3000 μm³. Error bars reflect uncertainties in the specific area measurements.

2019). This interpretation is supported by the higher CO₂-solid interfacial area at near-miscible conditions compared to immiscible conditions, see Fig. 12c and d.

3.5. Saturation and trapping

The saturation of water, oil and CO₂ in the macro pores was quantified after each injection step for both sets of experiments. The fluid saturations in Fig. 13 were measured on segmented images of the whole sample (4000 × 4000 × 20,000 μm³). After the first waterflooding (WF1), 46 ± 2% of the oil was recovered at immiscible conditions, while only 39 ± 2% was recovered for the near-miscible experiment. The discrepancy in the oil recovered through water injection in the two experiments is attributed to many reasons including the use of different rock samples, different fluids, and different temperatures and pressures, rather than the wetting state of the rock. However, the low oil recovery observed during WF1 in the two experiments is ascribed to water invading the centres of the pores, bypassing oil which resides in wetting layers in the corners and small pores. This is a common characteristic of oil-wet media (Salathiel, 1973).

Next, CO₂ was injected in a tertiary recovery process allowing the production of both oil and water. At immiscible conditions, this resulted

in a CO₂ saturation of only 24 ± 2%, while, at near-miscible conditions, the CO₂ saturation reached 33%; the injection of CO₂ at near-miscible conditions resulted in an additional oil recovery of 19 ± 2%, while at immiscible conditions only 9 ± 2% of extra oil was recovered. The higher oil recovery at near-miscible conditions is attributed to the negligible (low) gas-oil capillary pressure: as CO₂ invades the pore space it efficiently displaces all the oil it contacts (almost 100% microscopic displacement efficiency). The same favourable recovery has also been observed under near-miscible conditions in a water-wet rock (Alhosani et al., 2019).

Water injection during WF2 further reduces the oil and CO₂ saturations. At immiscible conditions, the subsequent injection of water is necessary to increase the oil production, an additional 14 ± 2% of oil was recovered during WF2; the injection of CO₂ alone is not sufficient to produce significant amounts of oil. Furthermore, water injection displaced only 5 ± 2% of the CO₂ saturation at immiscible conditions, while at near-miscible conditions the CO₂ saturation decreased by 12 ± 2%. The low CO₂ recovery at immiscible conditions is ascribed to the low connectivity of CO₂, CO₂ can form disconnected ganglia in the pore space, whereas, at near-miscible conditions, CO₂ exists in connected layers which allows the gas to be produced directly. This is also consistent with our interpretation that the principal displacement at

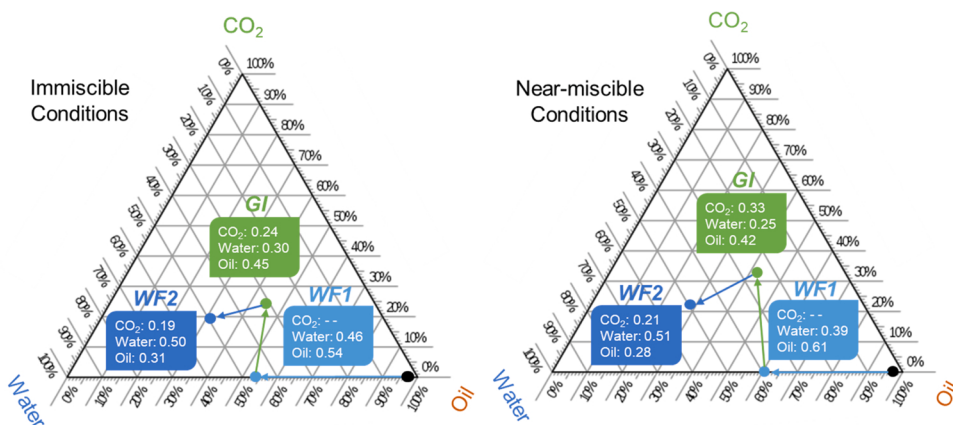


Fig. 13. Three-phase ternary diagrams showing the water, oil and CO₂ end-point saturations after each injection step at (left) immiscible conditions and (right) near-miscible conditions. At first (black point on the diagram), the rock is restored to its initial reservoir conditions (water saturation in macro pores: 0.01 and oil saturation: 0.99). The coloured arrows point to the chronological order of injection events: (i) first waterflooding [WF1]; (ii) gas injection [GI], and (iii) second waterflooding [WF2].

immiscible conditions is double drainage: water displaces disconnected CO_2 , but rather than being displaced, this CO_2 displaces oil in some of the larger pores, as discussed previously, see Fig. 7.

To recall, for CO_2 to become capillary trapped by another fluid phase in the centres of the pore space, in general it must be less wetting than that phase. Therefore, since CO_2 is more wetting to the rock than water at both immiscible and near-miscible conditions, this means that it cannot be capillary trapped by water. However, at immiscible conditions, CO_2 can coexist with oil in the same pore and it is less wetting than oil; hence, CO_2 can be capillary trapped by oil at these conditions. An example of this is illustrated in Fig. 14, where the injection of water during WF2 at immiscible conditions resulted in capillary trapping of CO_2 by oil. The CO_2 snap off was caused by oil that was displaced by water (Pickell et al., 1966; Sohrabi et al., 2004). In contrast, capillary trapping of CO_2 by oil is not possible at near-miscible conditions due to the low oil-gas capillary pressure, which prevents their direct contact in the pore space. This is confirmed by the lower Euler characteristic, see Table 6, after WF2, implying better connectivity.

3.6. Implications for recovery and storage

So far, we have demonstrated that although the wettability order, oil-gas-water from most to least wetting, is the same under immiscible conditions and near-miscible conditions, the pore-scale fluid configurations and trapping mechanisms remain different. Accordingly, we presume that the selected injection conditions (immiscible or near-miscible conditions) will have different implications on oil recovery and the safety of carbon dioxide storage in CO_2 -EOR projects. In our discussion of the results, the emphasis will be on local displacement efficiency – that is the amount of recovery and storage in parts of the pore space contacted by the injected fluids. Overall recovery will also, of course, be controlled by well placement and large-scale reservoir heterogeneity.

We suggest that at near-miscible conditions, an injection strategy of CO_2 injection only should be implemented for three reasons. (i) At near-miscible conditions, the flow of CO_2 in the pore space is restricted even when injected alone due to its existence in layers of low conductivity (Alhosani et al., 2020b). This means that it is difficult for the stored CO_2 to solely flow towards abandoned boreholes and escape through them. (ii) Significant amounts of oil can be recovered by CO_2 injection only at near-miscible conditions; the low gas-oil interfacial tension results in a high microscopic or local displacement efficiency. (iii) The subsequent injection of water produces significant quantities of the stored CO_2 , reducing the storage capacity; CO_2 exists in connected layers which allows the gas to be produced directly when displaced by water, albeit slowly. Water injection does not help to trap the CO_2 and simply

facilitates its displacement. Therefore, a continuous CO_2 injection only strategy is recommended at near-miscible conditions, or with minimal amounts of water – CO_2 is unlikely to be produced in significant quantities.

In contrast, to aid oil recovery and CO_2 storage during CCS-EOR at immiscible conditions, a WAG injection strategy is suggested. This is ascribed to two reasons. (i) CO_2 exists as disconnected ganglia in the pore space of the reservoir rocks; hence, the subsequent injection of water does not produce a large quantity of the stored CO_2 . Furthermore, at immiscible conditions, the injection of water can cause capillary trapping of CO_2 by oil in the centres of the pore space which is not possible at near-miscible conditions. Capillary trapping of CO_2 by oil ensures the safety of carbon storage. (ii) The injection of CO_2 alone at immiscible conditions is not sufficient to produce significant amounts of oil; subsequent water injection is necessary to increase the oil recovery.

4. Conclusions and future work

We have provided the first experimental evidence of three-phase displacement in strongly oil-wet reservoir rocks, where the wettability order in the system is altered such that water is the most non-wetting phase occupying the largest pores, oil is the most wetting phase occupying the smallest pores, while gas is the intermediate-wet phase occupying medium-sized pores. In our oil-wet rock, at immiscible conditions, we use micro-CT X-ray imaging to (i) characterize *in situ* contact angles and pore occupancy; (ii) examine fluid configurations and connectivity (Euler characteristic), (iii) investigate the formation of gas layers, (iv) quantify fluid-fluid/fluid-rock interfacial area; (v) measure fluid saturations during a WAG flooding strategy; and (vi) determine the carbon dioxide storage mechanism. We performed the same analysis on the near-miscible dataset, where the rock is slightly less oil-wet, obtained by Alhosani et al. (2020b), that has the same wettability order in the pore space, oil-gas-water from most to least wetting. Despite having the same wettability order, we observed distinct pore-scale phenomena at immiscible and near-miscible conditions.

Our main conclusions and implications from this work are:

- **CO_2 layers.** CO_2 as the intermediate-wet phase forms layers surrounding water at near-miscible conditions, while, at immiscible conditions, it exists as disconnected ganglia in the pore space. This is mainly due to the large negative gas spreading coefficient at immiscible conditions ($C_{sg} = -19.5 \text{ mN/m}$) which prevents it from spreading in layers compared to the near-miscible case ($C_{sg} = -2 \text{ mN/m}$). CO_2 can flow more readily in the pore space at immiscible conditions, when connected, as opposed to being confined to movement in layers at near-miscible conditions.

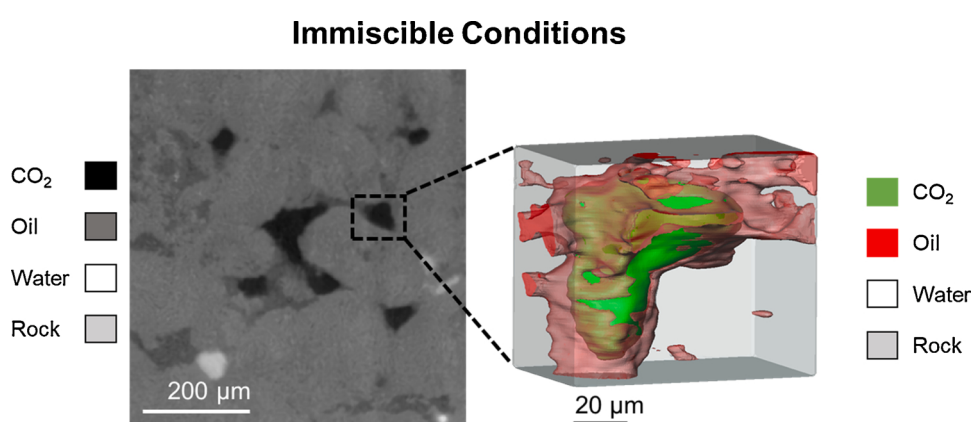


Fig. 14. (left) A $1.82 \mu\text{m}$ resolution pore-scale image showing capillary trapping of CO_2 by oil under strongly oil-wet immiscible conditions in a carbonate rock after the second waterflooding (WF2). (right) A selected 3D subvolume ($193 \times 126 \times 166 \mu\text{m}^3$) from (left) showing a trapped CO_2 ganglion surrounded by oil in a single pore.

- Capillary pressure.** As expected, the capillary pressure measurements displayed (-) negative oil-water and gas-water pressures and a (+) positive gas-oil pressure confirming the anticipated wettability order, oil-gas-water from most to least wetting, at both immiscible and near-miscible conditions. Despite having a similar gas-water capillary pressure in the two systems, the gas-oil capillary pressure was much higher at immiscible conditions due to its higher gas-oil interfacial tension.
- Interfacial area.** The CO₂-water specific interfacial area is higher at near-miscible conditions because of the spreading of CO₂ layers surrounding the water phase, whereas the CO₂-oil interfacial area is higher at immiscible conditions due to the trapping of CO₂ in the centres of the pore space by the oil wetting layers.
- Trapping.** Water, the most non-wetting phase, gets trapped in the centres of the pore space when CO₂ is injected at both conditions, with slightly higher water trapping at immiscible conditions. CO₂ is more connected at near-miscible conditions, albeit with a low flow conductance. Oil exists in thick wetting layers close to the rock surface at both conditions. It is not possible to capillary trap CO₂ by water in the centres of the pore space at both immiscible and near-miscible conditions since CO₂ is more wetting to the rock than water. However, capillary trapping of CO₂ by oil is possible at immiscible conditions.
- Oil recovery.** Near-miscible gas injection conditions are more favourable for oil recovery due to the low gas-oil interfacial tension which allows gas to displace oil efficiently from the pores (almost 100 % microscopic displacement efficiency).
- Implications for CO₂ storage.** Our results suggest that for favourable oil recovery coupled with effective CO₂ storage at near-miscible conditions during CCS-EOR, an injection strategy of CO₂ injection only should be implemented, while a WAG injection strategy (injection of CO₂ and water alternately) is recommended at immiscible conditions.

Future work should primarily focus on quantifying the relative permeabilities of water, oil and CO₂ in the pore spaces of water-wet, oil-wet and mixed-wet rocks at immiscible and near-miscible conditions. Moreover, a time-resolved synchrotron experiment can be conducted to better characterize the pore-scale dynamics of three-phase flow in oil-wet rocks. Furthermore, these results could be used to study energy balance and connectivity to help develop improved theories of three-phase flow in porous media.

Author statement

A.A. led the experimental work alongside A.S., Q.L. and E.A. under the supervision of M.J.B. and B.B. K.Z. performed interfacial tension measurements. A.A., A.S., Q.L., E.A., K.Z., B.B. and M.J.B. were involved in the design of the study, acquiring and analysing data, and writing the manuscript.

Data availability

The dataset analysed in this manuscript contains confidential images of a reservoir rock extracted from a large producing hydrocarbon reservoir in the Middle East. Approval to access the dataset can be requested by contacting the authors.

Declaration of Competing Interest

The authors declare that they have no known competing financial interests or personal relationships that could have appeared to influence the work reported in this paper.

Acknowledgments

We acknowledge Abu Dhabi National Oil Company (ADNOC) for funding this study.

Appendix A. Supplementary data

Supplementary material related to this article can be found, in the online version, at doi:<https://doi.org/10.1016/j.ijggc.2020.103232>.

References

- Akai, T., Lin, Q., Alhosani, A., Bijeljic, B., Blunt, J.M., 2019. Quantification of uncertainty and best practice in computing interfacial curvature from complex pore space images. *Materials* 12.
- Alhammadi, A.M., Alratrout, A., Singh, K., Bijeljic, B., Blunt, M.J., 2017. In situ characterization of mixed-wettability in a reservoir rock at subsurface conditions. *Sci. Rep.* 7, 10753.
- Alhammadi, A.M., Alratrout, A., Bijeljic, B., Blunt, M.J., 2018. Pore-scale imaging and characterization of hydrocarbon reservoir rock wettability at subsurface conditions using x-ray microtomography. *JoVE*, e57915.
- Alhosani, A., Scanziani, A., Lin, Q., Pan, Z., Bijeljic, B., Blunt, M.J., 2019. In situ pore-scale analysis of oil recovery during three-phase near-miscible CO₂ injection in a water-wet carbonate rock. *Adv. Water Resour.* 134, 103432.
- Alhosani, A., Scanziani, A., Lin, Q., Foroughi, S., Alhammadi, A.M., Blunt, M.J., Bijeljic, B., 2020a. Dynamics of water injection in an oil-wet reservoir rock at subsurface conditions: invasion patterns and pore-filling events. *Phys. Rev. E* 102, 023110.
- Alhosani, A., Scanziani, A., Lin, Q., Raeini, A.Q., Bijeljic, B., Blunt, M.J., 2020b. Pore-scale mechanisms of CO₂ storage in oilfields. *Sci. Rep.* 10, 8534.
- Alizadeh, A., Piri, M.J.W.R.R., 2014. The Effect of Saturation History on Three-phase Relative Permeability: an Experimental Study. 50, pp. 1636–1664.
- Alratrout, A., Raeini, A.Q., Bijeljic, B., Blunt, M.J., 2017. Automatic measurement of contact angle in pore-space images. *Adv. Water Resour.* 109, 158–169.
- Andrew, M., Bijeljic, B., Blunt, M.J., 2014a. Pore-by-pore capillary pressure measurements using X-ray microtomography at reservoir conditions: Curvature, snap-off, and remobilization of residual CO₂. *Water Resour. Res.* 50, 8760–8774.
- Andrew, M., Bijeljic, B., Blunt, M.J., 2014b. Pore-scale contact angle measurements at reservoir conditions using X-ray microtomography. *Adv. Water Resour.* 68, 24–31.
- Andrew, M., Bijeljic, B., Blunt, M.J., 2014c. Pore-scale imaging of trapped supercritical carbon dioxide in sandstones and carbonates. *Int. J. Greenh. Gas Control.* 22, 1–14.
- Arganda-Carreras, I., Kaynig, V., Rueden, C., Eliceiri, K.W., Schindelin, J., Cardona, A., Sebastian Seung, H., 2017. Trainable Weka Segmentation: a machine learning tool for microscopy pixel classification. *Bioinformatics* 33, 2424–2426.
- Armstrong, R.T., Porter, M.L., Wildenschild, D., 2012. Linking pore-scale interfacial curvature to column-scale capillary pressure. *Adv. Water Resour.* 46, 55–62.
- Bartell, F.E., Osterhof, H.J., 1927. Determination of the wettability of a solid by a liquid: relation of adhesion tension to stability of color varnish and lacquer systems. *Ind. Eng. Chem.* 19, 1277–1280.
- Blunt, M.J., 2001. Constraints on contact angles for multiple phases in thermodynamic equilibrium. *J. Colloid Interface Sci.* 239, 281–282.
- Blunt, M.J., 2017. Multiphase Flow in Permeable Media: a Pore-scale Perspective. Cambridge University Press.
- Blunt, M.J., Bijeljic, B., Dong, H., Gharbi, O., Iglauder, S., Mostaghimi, P., Paluszny, A., Pentland, C., 2013. Pore-scale imaging and modelling. *Adv. Water Resour.* 51, 197–216.
- Blunt, M.J., Alhosani, A., Lin, Q., Scanziani, A., Bijeljic, B., 2021. Determination of contact angles for three-phase flow in porous media using an energy balance. *J. Colloid Interface Sci.* 582, 283–290.
- Brown, K., Schlüter, S., Sheppard, A., Wildenschild, D., 2014. On the challenges of measuring interfacial characteristics of three-phase fluid flow with x-ray microtomography. *J. Microsc.* 253, 171–182.
- Bruant Jr., R.G., Celia, M.A., Guswa, A.J., Peters, C.A., 2002. Peer Reviewed: Safe Storage of CO₂ in Deep Saline Aquifers. *Environ. Sci. Technol.* 36, 240A–245A.
- Buades, A., Coll, B., Morel, J.-M., 2008. Nonlocal Image and Movie Denoising. *Int. J. Comput. Vis.* 76, 123–139.
- Buckley, J.S., 2001. Effective wettability of minerals exposed to crude oil. *Curr. Opin. Colloid Interface Sci.* 6, 191–196.
- CDP, 2020. Carbon Dioxide Properties Calculator [Online]. Available: <https://www.carbon-dioxide-properties.com/default.aspx> [Accessed 27/02/2020].
- Dicarlo, D.A., Akshay, S., Blunt, M.J., 2000. Three-Phase Relative Permeability of Water-Wet, Oil-Wet, and Mixed-Wet Sandpacks. *Spe J.* 5, 82–91.
- Dong, H., Blunt, M.J., 2009. Pore-network extraction from micro-computerized-tomography images. *Phys. Rev. E* 80, 036307.
- Edenhofer, O., 2015. IPCC Climate Change 2014: Mitigation of Climate Change. Cambridge University Press.
- First, P.J., 2018. Global Warming of 1.5 C an IPCC Special Report on the Impacts of Global Warming of 1.5 C Above Pre-industrial Levels and Related Global Greenhouse Gas Emission Pathways, in the Context of Strengthening the Global Response to the Threat of Climate Change, Sustainable Development, and Efforts to Eradicate Poverty.

- Garfi, G., John, C.M., Berg, S., Krevor, S., 2020. The sensitivity of estimates of multiphase fluid and solid properties of porous rocks to image processing. *Transp. Porous Media* 131, 985–1005.
- Heidug, W., Lippinen, J., Mccoy, S., Benoit, P., 2015. Storing CO₂ through enhanced oil recovery: combining EOR with CO₂ storage (EOR+) for profit. *Insight Series*.
- Herring, A.L., Harper, E.J., Andersson, L., Sheppard, A., Bay, B.K., Wildenschild, D., 2013. Effect of fluid topology on residual nonwetting phase trapping: Implications for geologic CO₂ sequestration. *Adv. Water Resour.* 62, 47–58.
- Herring, A.L., Andersson, L., Schlüter, S., Sheppard, A., Wildenschild, D., 2015. Efficiently engineering pore-scale processes: The role of force dominance and topology during nonwetting phase trapping in porous media. *Adv. Water Resour.* 79, 91–102.
- Herring, A.L., Robins, V., Sheppard, A.P., 2019. Topological persistence for relating microstructure and capillary fluid trapping in sandstones. *Water Resour. Res.* 55, 555–573.
- Iglauer, S., Paluszny, A., Rahman, T., Zhang, Y., Wülling, W., Lebedev, M., 2019. Residual trapping of CO₂ in an oil-filled, oil-wet sandstone core: results of three-phase pore-scale imaging. *Geophys. Res. Lett.* 46, 11146–11154.
- Jones, T.R., Carpenter, A., Golland, P., 2005. Voronoi-based segmentation of cells on image manifolds. In: Liu, Y., Jiang, T., Zhang, C. (Eds.), *Computer Vision for Biomedical Image Applications*. Springer, Berlin Heidelberg, pp. 535–543. Berlin, Heidelberg2005.
- Kaynig, V., Fuchs, T., Buhmann, J.M., 2010. Neuron geometry extraction by perceptual grouping in ssTEM images. 2010 IEEE Computer Society Conference on Computer Vision and Pattern Recognition 2902–2909, 13–18 June 2010.
- Khishvand, M., Alizadeh, A.H., Piri, M., 2016. In-situ characterization of wettability and pore-scale displacements during two- and three-phase flow in natural porous media. *Adv. Water Resour.* 97, 279–298.
- Kianinejad, A., Dicarlo, D.A., 2016. Three-phase oil relative permeability in Water-Wet media: a comprehensive study. *Transp. Porous Media* 112, 665–687.
- Kovsek, A.R., Wong, H., Radke, C.J., 1993. A pore-level scenario for the development of mixed wettability in oil reservoirs. *Aiche J.* 39, 1072–1085.
- Krevor, S., Blunt, M.J., Benson, S.M., Pentland, C.H., Reynolds, C., Al-Menhal, A., Niu, B., 2015. Capillary trapping for geologic carbon dioxide storage – from pore scale physics to field scale implications. *Int. J. Greenh. Gas Control.* 40, 221–237.
- Lake, L.W., 1989. Enhanced Oil Recovery.
- Leverett, M.C., Lewis, W.B., 1941. Steady flow of gas-oil-water mixtures through unconsolidated sands. *Trans. Aime* 142, 107–116.
- Li, X., Boek, E., Maitland, G.C., Trusler, J.P.M., 2012. Interfacial Tension of (Brines + CO₂): (0.864 NaCl + 0.136 KCl) at Temperatures between (298 and 448) K, Pressures between (2 and 50) MPa, and Total Molalities of (1 to 5) mol·kg⁻¹. *J. Chem. Eng. Data* 57, 1078–1088.
- Li, T., Schlüter, S., Dragila, M.I., Wildenschild, D., 2018. An improved method for estimating capillary pressure from 3D microtomography images and its application to the study of disconnected nonwetting phase. *Adv. Water Resour.* 114, 249–260.
- Lin, Q., Bijeljic, B., Pini, R., Blunt, M.J., Krevor, S., 2018. Imaging and measurement of pore-scale interfacial curvature to determine capillary pressure simultaneously with relative permeability. *Water Resour. Res.* 54, 7046–7060.
- Lin, Q., Bijeljic, B., Berg, S., Pini, R., Blunt, M.J., Krevor, S., 2019. Minimal surfaces in porous media: Pore-scale imaging of multiphase flow in an altered-wettability Bentheimer sandstone. *Phys. Rev. E* 99, 063105.
- Mecke, K.R., Wagner, H., 1991. Euler characteristic and related measures for random geometric sets. *J. Stat. Phys.* 64, 843–850.
- Metz, B., Davidson, O., De Cominck, H., Loos, M., Meyer, L., 2005. Carbon Dioxide Capture and Storage: Special Report of the Intergovernmental Panel on Climate Change. Cambridge University Press, 2005.
- NIST, 2019. Reference Fluid Thermodynamic and Transport Properties Database (REFPROP) [Online]. Available: <https://www.nist.gov/srd/refprop> [Accessed July 3, 2019].
- Núñez-López, V., Gil-Egui, R., Hosseini, S.A., 2019. Environmental and operational performance of co2-eor as a ccus technology: a cranfield example with dynamic lca considerations. *Energies* 12, 448.
- Oak, M.J., 1990. Three-Phase Relative Permeability of Water-Wet Berea. SPE/DOE Enhanced Oil Recovery Symposium. Society of Petroleum Engineers, Tulsa, Oklahoma.
- Oren, P.E., Billiotte, J., Pinczewski, W.V., 1992. Mobilization of waterflood residual oil by gas injection for water-wet conditions. *Spe Form. Eval.* 7, 70–78.
- Palaca, S., Socolow, R., 2004. Stabilization wedges: solving the climate problem for the next 50 years with current technologies. *Science* 305, 968.
- Pickell, J.J., Swanson, B.F., Hickman, W.B., 1966. Application of air-mercury and oil-air capillary pressure data in the study of pore structure and fluid distribution. *Old Spe J.* 6, 55–61.
- Qin, Z., Arshadi, M., Piri, M., 2019. Micro-scale experimental investigations of multiphase flow in oil-wet carbonates. II. Tertiary gas injection and WAG. *Fuel* 257, 116012.
- Raeini, A.Q., Bijeljic, B., Blunt, M.J., 2017. Generalized network modeling: network extraction as a coarse-scale discretization of the void space of porous media. *Phys. Rev. E* 96, 013312.
- Rudyanto, R.D., Kerkstra, S., Van Rikxoort, E.M., Fetita, C., Brillet, P.-Y., Lefevre, C., Xue, W., Zhu, X., Liang, J., Öksüz, I., Ünay, D., Kadipaşoglu, K., Estépar, R.S.J., Ross, J.C., Washko, G.R., Prieto, J.-C., Hoyos, M.H., Orkisz, M., Meine, H., Hüllebrand, M., Stöcker, C., Mir, F.L., Naranjo, V., Villanueva, E., Staring, M., Xiao, C., Stoel, B.C., Fabijanska, A., Smistad, E., Elster, A.C., Lindseth, F., Foruzan, A. H., Kiros, R., Popuri, K., Cobzas, D., Jimenez-Carretero, D., Santos, A., Ledesma-Carbayo, M.J., Helmerger, M., Urschler, M., Pienn, M., Bosboom, D.G.H., Campo, A., Prokop, M., De Jong, P.A., Ortiz-De-Solorzano, C., Muñoz-Barrutia, A., Van Ginneken, B., 2014. Comparing algorithms for automated vessel segmentation in computed tomography scans of the lung: the VESSEL12 study. *Med. Image Anal.* 18, 1217–1232.
- Salathiel, R.A., 1973. Oil recovery by surface film drainage in mixed-wettability rocks. *J. Pet. Technol.* 25, 1216–1224.
- Saraf, D.N., Batycky, J.P., Jackson, C.H., Fisher, D.B., 1982. An experimental investigation of three-phase flow of water-oil-gas mixtures through water-wet sandstones. In: SPE California Regional Meeting. San Francisco, California: Society of Petroleum Engineers.
- Sarem, A.M., 1966. Three-phase relative permeability measurements by unsteady-state method. *Old Spe J.* 6, 199–205.
- Scanziani, A., Alhammadi, A., Bijeljic, B., Blunt, M.J., 2018a. Three-phase flow visualization and characterization for a mixed-wet carbonate rock. In: Abu Dhabi International Petroleum Exhibition & Conference. Abu Dhabi, UAE: Society of Petroleum Engineers.
- Scanziani, A., Singh, K., Bultreys, T., Bijeljic, B., Blunt, M.J., 2018b. In situ characterization of immiscible three-phase flow at the pore scale for a water-wet carbonate rock. *Adv. Water Resour.* 121, 446–455.
- Scanziani, A., Singh, K., Menke, H., Bijeljic, B., Blunt, M.J., 2019. Dynamics of enhanced gas trapping applied to CO₂ storage in the presence of oil using synchrotron X-ray micro tomography. *Appl. Energy*, 114136.
- Scanziani, A., Alhosani, A., Lin, Q., Spurin, C., Garfi, G., Blunt, M.J., Bijeljic, B., 2020a. In situ characterization of three-phase flow in mixed-wet porous media using synchrotron imaging. *Water Resour. Res.* 56 e2020WR027873.
- Scanziani, A., Lin, Q., Alhosani, A., Blunt, M.J., Bijeljic, B., 2020b. Dynamics of fluid displacement in mixed-wet porous media. In: Proceedings of the Royal Society A: Mathematical, Physical and Engineering Sciences, 476, 20200040.
- Sohrabi, M., Tehrani, D.H., Danesh, A., Henderson, G.D., 2004. Visualization of oil recovery by water-alternating-Gas injection using high-pressure micromodels. *Spe J.* 9, 290–301.
- Stewart, R.J., Johnson, G., Heinemann, N., Wilkinson, M., Haszeldine, R.S., 2018. Low carbon oil production: enhanced oil recovery with CO₂ from North Sea residual oil zones. *Int. J. Greenh. Gas Control.* 75, 235–242.
- Toolbox, E., 2020. Carbon Dioxide - Dynamic and Kinematic Viscosity [Online]. Available: https://www.engineeringtoolbox.com/carbon-dioxide-dynamic-viscosity-temperature-pressure-d_2074.html [Accessed 28/08/2020]..
- Van Dijke, M.I.J., Sorbie, K.S., 2002. An Analysis of Three-Phase Pore Occupancies and Relative Permeabilities in Porous Media with Variable Wettability. *Transp. Porous Media* 48, 159–185.
- Van Dijke, M.I.J., Sorbie, K.S., 2003. Three-phase capillary entry conditions in pores of noncircular cross-section. *J. Colloid Interface Sci.* 260, 385–397.
- Van Dijke, M.I.J., McDougall, S.R., Sorbie, K.S., 2001a. Three-phase capillary pressure and relative permeability relationships in mixed-wet systems. *Transp. Porous Media* 44, 1–32.
- Van Dijke, M.I.J., Sorbie, K.S., McDougall, S.R., 2001b. Saturation-dependencies of three-phase relative permeabilities in mixed-wet and fractionally wet systems. *Adv. Water Resour.* 24, 365–384.
- Van Dijke, M.I.J., Lago, M., Sorbie, K.S., Araujo, M., 2004. Free energy balance for three fluid phases in a capillary of arbitrarily shaped cross-section: capillary entry pressures and layers of the intermediate-wetting phase. *J. Colloid Interface Sci.* 277, 184–201.
- Vogel, H.-J., 2002. Topological characterization of porous media. In: MECKE, K., STOYAN, D. (Eds.), *Morphology of Condensed Matter: Physics and Geometry of Spatially Complex Systems*. Berlin, Heidelberg: Springer, Berlin Heidelberg.
- Vogel, H.J., Kretzschmar, A., 1996. Topological characterization of pore space in soil — sample preparation and digital image-processing. *Geoderma* 73, 23–38.
- Wildenschild, D., Sheppard, A.P., 2013. X-ray imaging and analysis techniques for quantifying pore-scale structure and processes in subsurface porous medium systems. *Adv. Water Resour.* 51, 217–246.